Cape Peninsula
University of Technology

ANALYSIS OF LIFT AND DRAG FORCES ON THE WING OF THE UNDERWATER GLIDER

By

LUYANDA MILARD MEYERS

Thesis submitted in fulfilment of the requirements for the degree

Master of Engineering: Mechanical Engineering in the Faculty of Engineering at the
Cape Peninsula University of Technology

Supervisor: Dr Msomi

Co-supervisor: Prof MAE Kaunda

14/11/2018

DECLARATION

I, Luyanda Milard Meyers, declare that the contents of this dissertation/thesis represent my own unaided work, and that the dissertation/thesis has not previously been submitted for academic examination towards any qualification. Furthermore, it represents my own opinions and not necessarily those of the Cape Peninsula University of Technology.

_____ _____

Signed **Date**

ABSTRACT

Underwater glider wings are the lifting surfaces of unmanned underwater vehicles UUVs depending on the chosen aerofoil sections. The efficiency as well as the performance of an underwater glider mostly depends on the hydrodynamic characteristics such as lift, drag, lift to drag ratio, etc of the wings. Among other factors, the geometric properties of the glider wing are also crucial to underwater glider performance. This study presents an opportunity for the numerical investigation to improve the hydrodynamic performance by incorporating curvature at the trailing edge of a wing as oppose to the standard straight or sharp trailing edge. A CAD model with straight leading edge and trailing edge was prepared with NACA 0016 using SolidWorks 2017. The operating conditions were setup such that the inlet speed varies from 0.1 to 0.5 m/s representing a Reynolds number 27.8×10^3 and 53×10^3.

The static pressure at different angles of attack (AOA) which varies from 2 to 16degrees at the increment of 2degrees for three turbulent models (K-Ɛ-standard, K-Ɛ-RNG and K-Ɛ-Realizable), was computed for upper and lower surfaces of the modified wing model using ANSYS Fluent 18.1. Thereafter the static pressure distribution, lift coefficient, drag coefficient, lift to drag ratio and pressure coefficient for both upper and lower surfaces were analysed.

The findings showed that the lift and drag coefficient are influenced by the AOA and the inlet speed. If these parameters change the performance of the underwater glider changes as depicted by figure 5.6 and figure 5.7. The hydrodynamics of the underwater glider wing is optimized using the C_L/C_D ratio as function of the operating conditions (AOA and the inlet speed). The investigation showed that the optimal design point of the AOA of 12 degrees and a corresponding inlet speed of 0.26m/s. The critical AOA matched with the optimal design point AOA of 12 degrees. It was also observed that Cp varies across the wing span. The results showed the Cp is higher closer to the fuselage while decreasing towards the mid-span and at the tip of the wing. This showed that the wing experiences more stress close to the fuselage than the rest of the wing span which implies that a higher structural rigidity is required close to the fuselage. The results of the drag and lift curves correspond to the wing characteristics typical observed for this type of aerofoil.

ACKNOWLEDGEMENTS

TABLE OF CONTENTS

List of Figures

List of Tables

List of Notations & Abbreviations

C_L	Lift Coefficient
C_D	Drag Coefficient
C_L/ C_D	Drag polar
C_p	Pressure Coefficient
TE	Trailing edge (m)
LE	Leading Edge (m)
AOA	Angle of Attack (Degrees)
V	Velocity (m/s)
P	Pressure (pa)
F_D	Drag Force (N)
F_L	Lift Force (N)
ρ	Density (Kg/m^3)
AR	Aspect Ratio
µ	Kinematic Viscosity (m^2/s)
d	Diameter (m)
Dh	Hydraulic diameter (m)
Re	Reynolds Number
Ɛ	Epsilon
K	Constant
STD	Standard
UG	Underwater glider
AUV	Autonomous underwater vehicle
MSV	Manned Submersible Vehicle
ROV	Remotely Operated Vehicle
CFD	Computational Fluid Dynamics
RANS	Reynolds Average Navier-Stokes Simulation
DNS	Direct Numerical Simulation
LES	Large Eddy Simulation
CAD	Computer Aided Draughting
RNG	Renormalizing group
FDM	Finite Difference Method
FVM	Finite Volume Method
FEM	Finite Element Method

CHAPTER 1

INTRODUCTION

In the early days, scientists through curiosity started searching the ocean with the mission to explore the marine life, minerals and make discoveries. In the absence of technology, humans were trained as divers to fulfil this mission. The nature of the work was to dive with some equipment to collect samples on the sea floor and back to the dock station, where further analysis or research was conducted. This unfortunately comes with a price, since sea life is not as friendly as we think; this made such missions costly and dangerous.

This then underpinned the invention of underwater robots, which could be deployed anywhere in the marine environment to bring samples with less risk and at a faction of the cost associated with the use of human divers. These robots are generally classified into manned submarine vehicles (MSV), remotely operated vehicle (ROV), autonomous underwater vehicle (AUV) and underwater glider (UG). Even though there was progress in the technological developments in this field, the vehicles have limitations in terms of cost, operating time and manpower. The limits differ depending on the vehicle class e.g. ROV are tethered vehicles, controlled by operators with high manoeuvrability advantage, and results in less constraint compared to the MSV. The AUV's are autonomous and can be deployed in the marine environment with no manpower and tethering. The vehicle is battery powered, which enables it to run autonomously to accomplish the required mission. By contrast, underwater glider has no propulsion system everything is control inside, moving at a relatively slow speed compared to the AUV, with longer duration and range.

1.1 PROBLEM STATEMENT

Underwater gliders are self-propelled unmanned underwater vehicle with fixed wings that convert vertical motion into horizontal motion, (Javaid et al., 2017). The vehicle has no external propellers it gains its propulsion internally, by shifting negative to positive buoyancy using the submarine mechanism, where it gains downward motion by additional mass or vice versa for surfacing using piston pumps. Since the vehicle has no external propellers, the guide path is controlled by external planes (wings) resulting in a trajectory of a sawtooth path or sinusoidal as shown in figure1.1
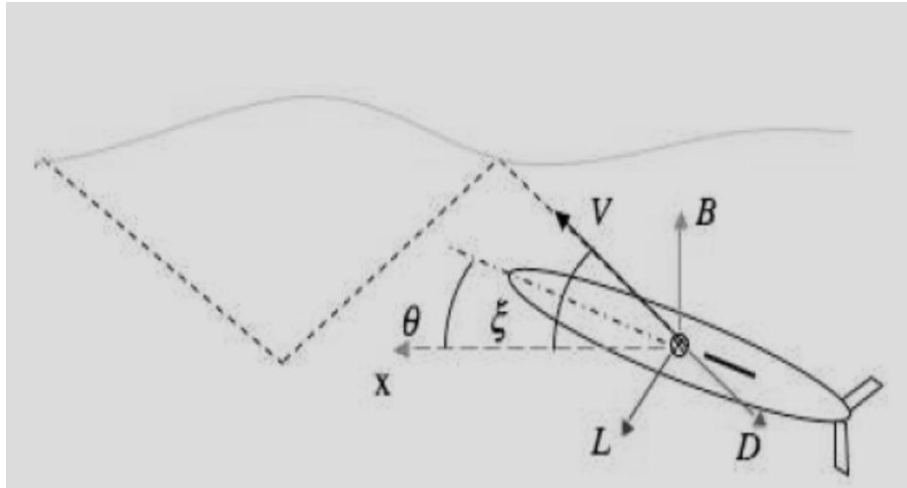
Figure 1-1 Underwater glider operation-sawtooth path Bender et al., (2006)

Zhang et al., (2013), carried out an investigation on a simple non-standard trapezoid wing at different wing aspect ratio (Zhang et al., 2013). The findings showed larger wings result in shallow gliding path, longer horizontal travel with slow speed as compared to the smaller wings. Liu et al., (2014), looked at the effect of the wing layout, specifically the influence of the chord length, aspect ratio, sweep back angle and axial position. Their findings showed that the chord length has a significant impact on the lift to drag ratio, while sweep angle has significant impact on the movement of the underwater glider.

This present study looks at the effect of underwater glider wings geometric design with the aim addressing the shortcomings experienced by current existing glider wings shapes as mentioned above by introducing a Controlled Volume Computational Modelling technique to compute the hydrodynamic forces acting on the glider wings.

1.2   BACKGROUND TO THE RESEARCH PROBLEM

At the end of world war two, designs of wings were of extreme importance, each institution conducted their own investigation by testing various wing shapes and designs (Abbott, n.d.).This process was carried out experimentally using wind tunnels in conjunction with empirical methods. However due to the extraordinary and fine work done by NASA team, their work was rated the most outstanding and reliable at that time (Abbott, n.d.). Since then most traditional wing design were influenced by NACA's pioneering work and their designs were used as reference point. The traditional NACA wings designs shape has a round leading edge and sharp trailing edge.

A study on the effect of the trailing edge was conducted by (Gómez & Pinilla, 2006) to see the aerodynamic effect of the blunt trailing edge as oppose to the traditional sharp trailing edge.

The modification was parameterized by cutting the trailing edge perpendicular in different sections along the chord length as depicted in figure 1.2. The findings showed an increase in the maximum lift coefficient, profile drag and lift coefficient slope.
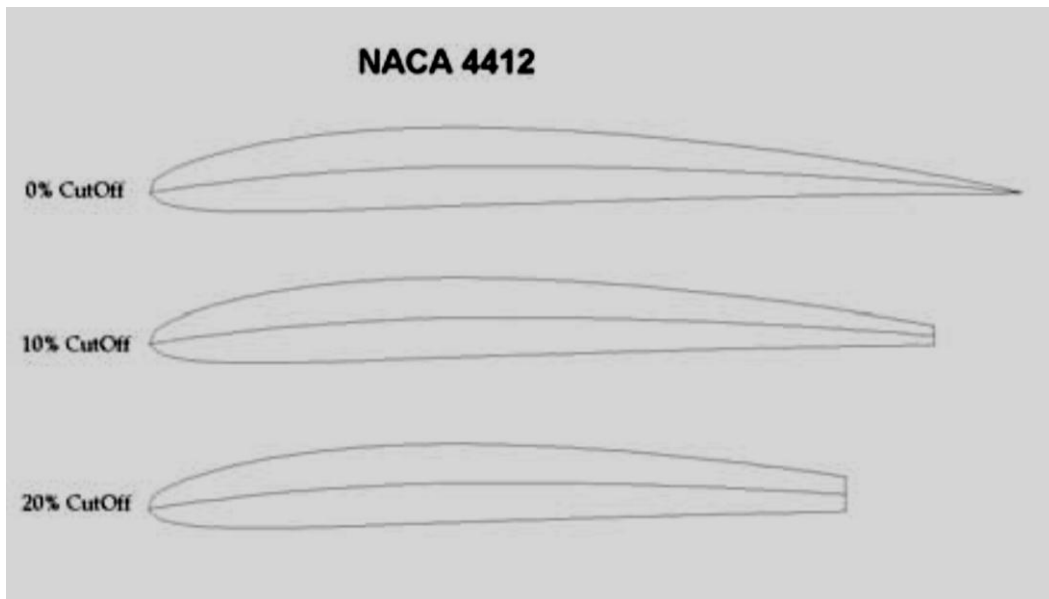
Figure 1-2 Modified NACA4412 aerofoil (Gómez & Pinilla, 2006)

A similar study was also conducted by (Thomareisa & Papadakis, 2017) using a numerical approach to study the effect of the trailing edge on separated flow characteristics around an aerofoil in low Reynolds numbers and with of separating shear layer. The NACA0012 aerofoil with standard straight trailing edge performance was investigated in comparison with the blunt trailing edge and serrated trailing edge as depicted by figure 1.2 and figure 1.3.
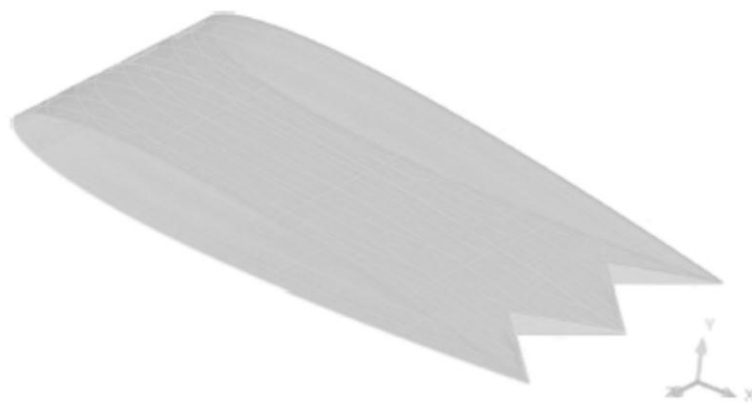
Figure 1-3 Serrated trailing edge(Thomareisa & Papadakis, 2017)

The findings showed that the traditional straight-line standard aerofoil recorded two modes: High frequency which corresponds to Kelvin Helmholtz instability originating from the separated shear layer and low frequency which emerges as a sub-harmonic, detectable at the suction side and near the wake.

The blunt trailing edge showed two shear layer frequencies which are strongly suppressed and the frequency of the shear layer is locked to the shedding frequency due to exposed bluntness. Serrated trailing edge which consist of triangular serration as shown in figure 1.3. The strength of the vortices shed from the exposed blunt part is strongly attenuated compared to the flatback aerofoil and this results in the presence of both sub-harmonic and shedding frequency in the velocity spectra in the wake as well as in the suction side of the aerofoil

Xie et al., (2013) undertook a similar study looking at the effect of the incident angle on the gliding distance of the glider. The smaller the gliding angle the longer the gliding distance, but due to the relationship between the gliding angle and the wing incident angle, it is not easy to measure the gliding angle directly (Xie et al., 2013). Thereafter, passively rotatable wings were proposed. The findings showed that the passively rotatable wings can achieve a longer range than the conventional fixed-wings if the incident angle is set properly.

The investigation of aerofoil has been reported in many studies whereby flapping, blunt and serrated trailing edges were investigated with the aim of gaining lift and reducing drag. However, there are very few studies on the effect of the round trailing edge on the hydrodynamic performance of the underwater glider. This study is structured according to the work conducted by (Javaid et al., 2016) where they looked at the effect of the wing form on the hydrodynamics of the underwater glider i.e. tapered and rectangular wing using standard NACA0016 aerofoil. This study looks at the effect of the rectangular wing form with round trailing edge as opposed to the standard straight or sharp trailing edge, using the standard NACA0016 as well. The investigation looks at the influence of the inlet speed and angle of attack (AOA) on the hydrodynamic parameters such as coefficient of lift (C_L), coefficient of drag (C_D), coefficient of pressure and the drag polar (C_D/C_L)) as a result of the geometric modification of the trailing edge of the underwater glider wing.

1.3   AIM

The aim of the study is to find alternatives wing shapes that can improve the performance of the underwater glider as oppose to the current traditional sharp trailing edge wing form.

1.4   OBJECTIVES

The main objectives of this thesis are to investigate the hydrodynamic performance of the glider wing using the coefficient of lift (C_L), coefficient of drag (C_D), coefficient of pressure (Cp) and drag polar (C_D/C_L) as parameters of interest.

1.5   STRUCTURE OF THE THESIS

CHAPTER 1

This chapter introduce the research, background to the research problem, aim of the project and its objectives and lastly gives the layout of the thesis.

CHAPTER 2

Chapter two covers the literature review of the research area, underwater robots, oceanographic engineering, the classification of autonomous Underwater Vehicles (AUV's) and the numerical and experimental studies on the wings form.

CHAPTER 3

Chapter three covers basic mathematical concept of CFD looking at the governing equations, overview of the Computational Fluid Dynamics (CFD), numerical methods, turbulence and hydrodynamic models.

CHAPTER 4

Chapter four's focus is on the research methodology which discuss the glider wing geometric design, flow domain creation, the computational mesh, brief theoretical considerations on thin aerofoil and wings, turbulence resolutions and lastly numerical solutions.

CHAPTER 5

Chapter five covers the discussions of the results using qualitative and quantitative plots respectively.

CHAPTER 6

This chapter covers the conclusions on the findings and possible recommendations for future work.

CHAPTER 2

LITERATURE REVIEW

The study of the ocean became more popular since 19th century where the interest to explore the ocean treasure grew stronger. As we all know the danger of the ocean to human kind, scientist used sensors and floats to collect data but the shortcomings with this approach was the range, duration and man power requirements. This forced the oceanographers to explore the use of underwater vehicles. Underwater vehicles are small robots deployed from the ship into the ocean with predefined mission based on the payload. Underwater vehicles are designed with the intension to complete three tasks namely oceanographic sampling, exploration and observation (Raj et al., 2014).

These class of vehicles are subdivided into, Autonomous Underwater Vehicle (AUV), Remotely Operated Underwater Vehicle (ROV) and Underwater Glider (UG). This study will be focusing more on underwater gliders.

2.1   BACKGROUND OF UNDERWATER GLIDERS

In 1989, Oceanographer Henry Stommel envisioned a future of underwater robots, working in a group, autonomously powered by a sort of buoyant energy. This vision was put forward by other oceanographers in 2001, three underwater gliders were developed by three different institutions. Doug Webb and his team via Webb Research Cooperation developed two types of Slocum underwater gliders (electrically powered and thermal powered). Scripps Institution of oceanography developed Spray underwater glider named after Joshua Slocum sail boat by honouring the first brave man to sail around the world in small boat and University of Washington developed Sea glider (Hussain et al., 2011). The detailed specifications of the three popular underwater gliders are shown in table 2.1.

Table 2-1 Comparison of specifications between Spray, Slocum and Seaglider (Davis et al., 2002)

Spray	Specifications
Hull	Length 2m, Diameter 0.2m, Mass 51 kg, Payload 3.5 kg
Lift Surfaces	Wing span (Chord) 1.2 (0.1) m, Vertical stabilizer length (chord) 0.49(0.07) m
Volume Change	Max 900 cc, Motor & reciprocating pump, 50 (20) % efficient @1000(100) dbar
Communication	Iridium, 180 byte/s net, 35 J/Kbyte. GPS navigation
Operating	Max P 1500 dbar, Max U 45 cm/s, Control on depth+altitude+vertical W
Endurance	U = 0.27m/s, 180 glides, Buoyancy 125 gm, Range 7000 km, Duration 330 days
Slocum	
Hull	Length 1,5m (overall 215), Diameter 0.21m, Mass 52kg, Payload 5 kg
Lift Surfaces	Wing span (chord) 1.2 (0.09) m swept 45^0, Stabilizer length (chord) 0.15 (0.18) m
Volume Change	Typical 450 cc, 90 W motor & single-stroke pump, 50% efficient @200 dbar
Communication	Freewave LAN,5.7 Kbytes/s, 3 J/Mbyte, 30 km range – or –Iridium, GPS navigation
Operating	Max P200 dbar, Max U 0.4m/s, Control on depth+altitude+altitude+vertical W
Endurance	U = 0.35m/s, 25^0 glides, Buoyancy 230 gm, Range 500 km, Duration 20 days
Seaglider	
Hull & Shroud	Length 1.8 m(Overall3.3), diameter 0.3m, Mass 52kg, Payload 4kg
Lift Surfaces	Wing span (av chord) 1(0.16) m, Vertical stabilizer span (chord) 0.4 (0.07) m
Volume Change	Max 840 cc, Motor & reciprocating pump,40% (8%) efficient at 1000(100) dbar
Communication	Iridium,180 bytes net, 35J/Kbytes, GPS navigation
Operating	Max P 1000 dbar, Max U 0.45m/s, Control on depth+position+attitude+vertical W
Endurance	U= 0.27 m/s, 16^0 glides, buoyancy 130gm, Range 4600 km, Duration 200days

Underwater gliders are self-propelled unmanned underwater vehicle with wings that convert vertical motion into horizontal motion, Javaid, M.Y, et al., (2016). The vehicle has no external propellers it gains its propulsion internally, by shifting negative to positive buoyancy using the submarine mechanism, where it gains downward motion by additional mass or vice versa and for surfacing use piston pumps or ballast tanks. Since the vehicle has no external propellers manoeuvrability is largely by external planes(wings). This then result in a trajectory of a sawtooth path or sinusoidal motion. Bender and his colleagues (Bender et al., 2008), describes underwater gliders as a type of autonomous submersibles vehicles with an approximate length of 2 metres, weighing 50 kilograms and resembling sailplanes as shown

in figure 2.1. According to Hussain et al., (2011), the existing gliders are designed with fixed wings and tails.
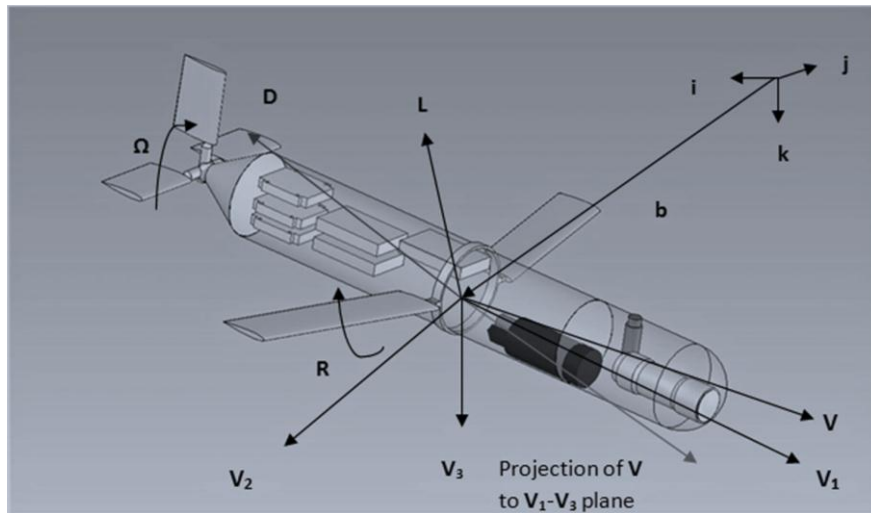
Figure 2-1 Glider dynamics (Hussain et al., 2011)

2.2 UNDERWATER GLIDER CHARACTERISTICS AND APPLICATIONS

According to Singh et al., (2017) underwater gliders can travel kilometres underwater before re-surfacing and with this capability they can be deployed in a wide range of tasks where it is difficult for shipboard to take measurements. The most popular use of the underwater gliders includes scientific data collection, ecological protection, defence or naval applications. In scientific applications underwater gliders are used for measuring temperature, conductivity, current speed and direction, depth, optical backscatter, acoustic backscatter, chlorophyll fluorescence etc. In defence they are used for maritime intelligence surveillance and reconnaissance, mine detection, anti-submarine warfare, real time command, control and communications and harbour patrolling.(Singh et al., 2017)

2.3 STUDIES CONDUCTED ON UNDERWATER GLIDERS

There is an ongoing research conducted on underwater gliders whereby more time is invested to study the hydrodynamics of the vehicles with the goal of improving its performance in terms of range, duration and manoeuvrability. The amount of time the AUV's can stay underwater determines its endurance. Since underwater vehicles are designed to take marine samples, inspection of the ship hull, underwater pipes inspection etc. AUV spent considerable amount

of time underwater without refuelling or charging hence a good propulsion technique, better speed and energy source is needed (Raj & Chandra, 2014).

Underwater gliders have no propulsion power which makes it unique compared to other AUV and with better endurance (Hussain et al., 2011). The lack of propulsion power result in less energy usage making it possible to operate at much deeper depth, like the sea glider. This type of underwater vehicle has low drag hull with high lift to drag ratio. Therefore the proper wing configuration is crucial to minimise the drag and optimise energy consumption.(Singh et al., 2017)

There are different approaches used to study the hydrodynamics of this vehicle but with the advances in computational power, the most common approach is by numerical simulation using (CFD) platform validated by experimental data.

2.3.1 The influence of the wing shape on lift and drag characteristics

2.3.1.1 Theory of wings

The systematic tests were done by National Advisory Committee for Aeronautical (NACA) on various shapes of the aerofoils generating data for aircraft design. Although these test were conducted many decades ago but are still used as the reference guide even today when designing certain components of the aircraft.(Anon, n.d.) The NACA produced different family of wings , ranging from 4- digit ,5 digit and 6-digit aerofoils. The specifications of these wings are shown in table 2.2.

Table 2-2 Classification of different NACA family of wings (Anon, n.d.)

Series type	NACA Type	Camber $_{max}$	Thickness $_{max}$
4 digits	NACA2415	0.02% over the chord	0.15c
5 digits	NACA23021	0.02% over the chord	0.12c
6 digits	NACA63215	-	0.15c

The shape of the standard NACA wing follows a round leading edge (LE) and a sharp trailing edge (TE) as mentioned in section 1.3. Since the work deals with the four-digit wing, the numbering system for the four-digit series is based on the section geometry. The first integer indicates the maximum value of the mean-line coordinate in percent of the chord while the second integer represent the distance from the LE to the maximum camber in tenths of the chord. The last two integers indicate the section thickness in percent of the chord. In cases of

10

the NACA 0016, this type of wing is symmetrical due to the first two zero's in front sections and the last two integers represents the percentage thickness. (Abbott, n.d.)

2.3.1.1.1 Wing aspect ratio

The wing aspect ratio is known as the wing span divided by the geometric chord or it can be described as the measure of how long and narrow the wing is.(Anon, n.d.).The formula to calculate the aspect ratio is given by equation 2.1.

$$AR = \frac{b}{c} = \frac{b^2}{S} \qquad\qquad (2.1)$$

The early wind tunnel test showed the rate of change of the lift and drag coefficients as a function of the AOA are strongly affected by the aspect ratio of the model.(Abbott, n.d.).

2.3.1.2 Experimental approach

This study deals with external flow around underwater glider wing. The nature of the flow in the fluid is determined by the Reynolds number. This parameter is a function of speed, density, viscosity and the surface area as shown by equation.

$$Re = \frac{\rho v d}{\mu} \qquad\qquad (2.2)$$

According Hussain and his team (Hussain et al., 2011), underwater gliders speed ranges between 0.25 m/s to 0.5 m/s. The nature of the speed of the underwater gliders in respect to equation 2.2 suggest that the flow around these vehicles is turbulent. The flow in this region is chaotic and three dimensional and results in fluctuating flow behaviour. Since this study deals with external flow, there are ample studies conducted on hydrodynamics characteristics around underwater gliders with the aim of improving the performance in terms of range, endurance, stability and reduction of the operating cost. The primary focus of this chapter will be directed towards the influence of the wing form shape on the hydrodynamic characteristics of the underwater glider.

(Dod, 1946), conducted an experimental study on a wind tunnel for various NACA 44 series wings looking at the aspect ratio, taper ratio and overall surface finish of the wing. His approach used the experiment data to validate the computed aerodynamics characteristics of the wings. The calculations were carefully done by considering different methods which use

lifting-line theory which assumes linear section of lift curves and the non-linear lift curves theory.

The findings for both methods of calculation showed reasonable agreement with the experiment data for the wing force (drag) and the moment characteristics. However, the method that allows the use of nonlinear lift curves gave better agreement with the experiments at high AOA. The only point where both methods gave different results was on the span wise lift distributions at maximum lift. The results also compared the drag and lift force at an equal Reynolds number for all the conditions and the findings showed that the lift to drag ratio for smooth wings increased with the increasing aspect ratios throughout the wing span irrespective of the increase in drag due to the increasing root thickness at higher aspect ratios.

The (L/D) $_{max}$, for the taper ratio of 3.5 with rough leading-edge surface yielded the same trend with smooth surface wings, however for the taper ratio of 2.5 with same surface finish showed no gain when the aspect ratio was increased from 10 to 12. Lastly, the maximum lift coefficient decreased with increasing aspect ratio due to the increase in root thickness to chord ratio.

Haque et al.,(2015) conducted a similar study where they performed a test experimentally on NACA 4412 using wind tunnel (Haque et al., 2015). The test compared the aerodynamic performance by incorporating a curvature in the leading-edge while maintaining the straight trailing edge in comparison with a rectangular straight leading-edge and straight trailing-edge as shown in figure 2.2.
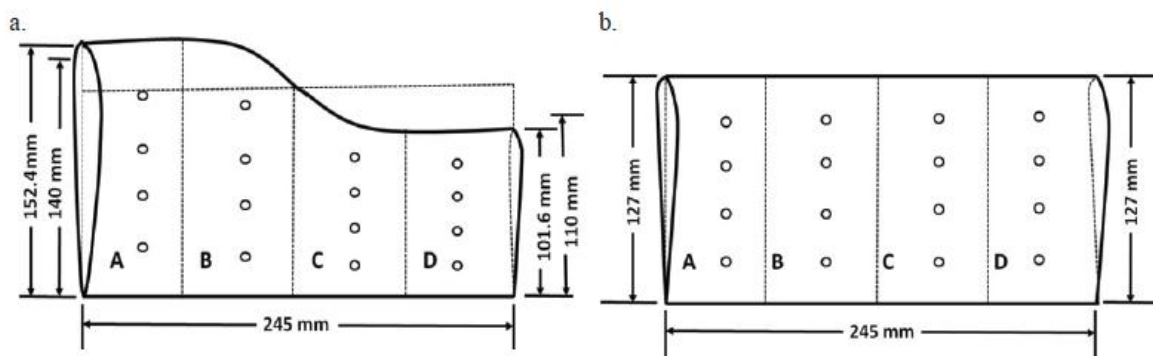
Figure 2-2 (a) Curved Leading Edge Planform (b) Rectangular Planform (Haque et al., 2015)

The findings show the curved leading-edge wing planform exhibit high lift coefficient and lower drag coefficient than the rectangular wing planform. This also result in curved leading-edge planform having higher lift to drag ratio than the rectangular planform. The other finding showed the pressure coefficient is independent of the chord length, by displaying the variation of the Cp while maintaining the chord length constant.

Hossain et al.,(2011) conducted an experiment on aerodynamic characteristics of the rectangular wing with and without bird feather like winglets for different Reynolds Numbers (Hussain et al., 2011). The findings showed 25-30% reduction in Cd and 10-20% increase in Cl for the bird feather like winglet at AOA of 8 degrees. Dwivedi et al., (2018) also adopted an experimental approach in studying different wing shapes i.e. Rectangular, rectangular with curved tip, tapered, tapered with curved tip for low speed at various AOA. The findings showed tapered wing with curved tip exhibit the best aerodynamic stability for various speed and AOA(Dwivedi et al., 2018).

2.3.1.3 Numerical approach

The lift generated by the wing sustains the weight of the underwater glider to sustain its motion in water. There are different numeral approaches used to investigate the influence of the wing form using different Computational Fluid Dynamics (CFD) platforms. According to Lynch (1982) around two thirds of the total drag of the aircraft or submersible is produced by wings hence the wing form shape is very crucial to the performance of a glider.

A numerical study was conducted by (Ahmed, 2013) looking at the flow around a NACA0012 wing flapped at different flap angles with varying Mach Numbers. The study used k-ω shear stress transport (SST) turbulence model to predict the flow accuracy along with turbulence intensities 1% and 5% at different inlet velocities and pressure outlet respectively. The findings showed that the calculation of C_L, C_D and C_L/C_D ratio at different operating conditions with the increase in Mach number, C_L increases whereas C_D remain constant. It was also noticed as the speed approaches sonic velocity, a rapid decrease in C_L was observed whereas an abrupt upsurge was observed for C_D.

A study by Arvin et al.,(2016) on 3D simulation of turbulent flow over three different aerofoils (NACA 680094 ,NASA-GAW2 and a designed aerofoil) was conducted (Arvin et al., 2016). Two computational platforms: ANSYS-fluent and XFLR5-V609 were used to carry out the investigation looking at the effect of Moment coefficient (Mc), C_L and drag coefficient C_D for various AOA and Reynolds numbers. The findings showed that the designed aerofoil exhibit similar behaviour with the standard aerofoil for different AOA and resulting C_L / C_D ratio at AOA of 5 degrees.

Rahimi et al.,(2014) undertook a study on numerical investigation of 2D and 3D for different aerofoils at Laminar and Turbulent flow conditions using Open FOAM (Rahimi et al., 2014).

The findings showed good agreement when compared to the experimental data and other numeral results for both Open FOAM transition model and k-ω (SST).

Jones & Clarke,2005 conducted a numerical study using the CFD code (Fluent) to cary the investigation of horseshoe vortex formed in a typical wing junction in a turbulent flow experiment using various turbulent models i.e. k-Ɛ (RNG) ,Reynolds stress model(RSM ,V2F model, Spallart – Allmaras model and k-ω model.The findings showed ,the k-Ɛ (Realizable) model predictions is less accurate when compared to all other models for mean velocity compents.None of the models predicted accuratetly the behavior of the mean kinetic energy as a function of the domain extent although for time averaged velocity components most locations the models predicited these components accurately.

A numerical simulation of the aerofoil flow at high AOA was conducted by (Panaras, 2015).The study look at different turbulent models i.e linear k-ω (SST), non-linear algebraic Stress Model and Baldwin-Lomax model. The findings showed that the tested models captured the physics of unsteady seperated flow.Good agreement between computational and experimental surface pressure data was also observed.

According to Azim et al.,(2015) the flow separation at the trailing edge of the aerofoil affects the aerodynamic perfomance significantly (Azim et al., 2015).For instance, a decrease in the lift whilst increasing the drag.Their study looked at the boundary layer separation using 2D NACA 4412 model by introducing suction on the aerofoil and use CFD to compute the numerical results.The right suction position is paramount and therefore the aerofoil was slotted with a width of 2% of the chord length in five different positions starting from 48% to 70% of the chord length.The findings showed that if the suction pressure is kept at 65 kpa at 68% of the chord length at the AOA = 13 degrees, it is possible to arrive at an optimal position where the suction inside the aerofoil works best. The delay in the onset of the turbulent flow ultimately results in an increase in the lift.

In a simlar study (van de Wal, 2010), studied the design of the wing with boundary layer suction with the aim of reducing the profile drag.The study designed a completely new aerofoil in XFOIL and optimized the design for boundary layer suction.The new aerofoil produced good results with or without suction and reduced the profile drag tremendously while on the other hand the lift coefficient increased dramatically.

In another investigation (Fulvio Bellobuono Tutor Coordinator Domenico Coiro Antonio Moccia, 2006), a study was conducted on exploring different ways of achieving efficient boundary layer control, with an awareness of the practical implications when installing the device on the actual wing.The study also look at the verification of the existing active control steady suction and pulse blowing to see which one is effective in terms of boundary layer

separation.The findings showed that the steady suction is an effective tool for delaying the boundary layer seperation, but it is a function of the position of the slot, whereas the numerical and experimental test showed that the unsteady blowing is more effective than the steady blowing.

2.4 SUMMARY

Looking at the litearture that has been reviewed in this chapter, it became evident that there is very minimal work done around the subject of optimization of underwater glider wings.This has brought the need of studying the effects of hydrodynamic perfomance of an underwater glider looking at the effect of modifying the trailing edge of the underwater glider wing.The recent Literature has revealed that most work has been perfomed through the analysis of the perfomance of the entire wing shapes i.e. Tappered wings against rectangular wings,perforated wing using active control steady suction and pulse blowing. This work is analysing the effect of modifying the trailing edge of the recctangular NACA0016 wing shape.

CHAPTER 3

COMPUTATIONAL FLUID DYNAMICS (CFD)

Computational Fluid Dynamics (CFD) is the branch of Fluid mechanics that deals with the analysis of systems involving fluid flow, heat transfer and associated phenomena such as chemical reactions by means of computer-based simulation. The technique is very powerful and widely used in many academia, industries and in non-industrial applications. In the early 1960s aerospace extended the capability of the technique to iterate the design, research and development (R&D) and overlapping functions to the manufacturing of aircraft and jet engines.

3.1. GOVERNING EQUATIONS

The principles of conservation of mass, energy and momentum are used to derive the fundamental equations necessary to describe the behaviour of any fluid flow. Since this work deals with incompressible fluid it is assumed that solving the energy equation will have no significant effect on the solution, therefore the heat transfer during the fluid flow is neglected to simplify the problem.

The governing equations for incompressible flow are based on the conservation equations of mass and momentum. These equations which are solved using numerical methods is given in a three-dimensional differential form as shown below (Versteeg and Malasekera, 2007).

3.1.1 Mass conservation equation

The three-dimensional mass conservation for incompressible fluid is given by equation (3.1).

$$\frac{\partial u}{\partial x} + \frac{\partial v}{\partial y} + \frac{\partial w}{\partial z} = 0 \tag{3.1}$$

where $u = \frac{dx}{dt}; v = \frac{dy}{dt} \ and \ w = \frac{dz}{dt}$ are the velocities in the different positions of the three-dimensional axis x, y and z.

Equation (3.1) in more compact vector notation is given by equation (3.2)

$$\text{div } \mathbf{u} = 0 \tag{3.2}$$

where $\text{div } \mathbf{u} = \frac{\partial u}{\partial x} + \frac{\partial v}{\partial y} + \frac{\partial w}{\partial z}$

3.1.2 Momentum conservation equation

The momentum conservation equation is shown by equation (3.3).

$$\frac{D\varphi}{Dt} = \frac{\partial\varphi}{\partial t} + \frac{\partial\varphi}{\partial x}\frac{dx}{dt} + \frac{\partial\varphi}{\partial y}\frac{dy}{dt} + \frac{\partial\varphi}{\partial z}\frac{dz}{dt} \tag{3.3}$$

Equation 3 can also be written as shown in equation (3.4)

$$\frac{D\varphi}{Dt} = \frac{\partial\varphi}{\partial t} + u\frac{\partial\varphi}{\partial x} + v\frac{\partial\varphi}{\partial y} + w\frac{\partial\varphi}{\partial z} = \frac{\partial\varphi}{\partial t} + \boldsymbol{u}.\,grad\varphi \tag{3.4}$$

where $grad\varphi = \frac{\partial\varphi}{\partial x} + \frac{\partial\varphi}{\partial y} + \frac{\partial\varphi}{\partial z} = \frac{\partial\varphi}{\partial t}$

Therefore, the x-momentum, y-momentum and z-momentum for incompressible flow then becomes:

$$\frac{\partial u}{\partial t} + \text{div}(u\boldsymbol{u}) = -\frac{1}{\rho}\frac{\partial p}{\partial x} + v\,\text{div}(grad(u)) \tag{3.5}$$

$$\frac{\partial v}{\partial t} + \text{div}(v\boldsymbol{u}) = -\frac{1}{\rho}\frac{\partial p}{\partial y} + v\,\text{div}(grad(v)) \tag{3.6}$$

$$\frac{\partial w}{\partial t} + \text{div}(w\boldsymbol{u}) = -\frac{1}{\rho}\frac{\partial p}{\partial z} + v\,\text{div}(grad(w)) \tag{3.7}$$

3.2 CFD MODELLING TECHNIQUES

In general, there are three computational approaches available to model the behaviour of turbulent flow namely: Direct Numerical Simulation (DNS), Large Eddy Simulation (LES) and Reynolds Average Navier-Stokes Simulation (RANS). A brief explanation of each approach will be discussed and closed off with a numerical approach suitable for the nature of the problem investigated.

3.2.1 Direct numerical approach (DNS)

Direct numerical simulation computes both the mean flow and all turbulent velocity fluctuations. The unsteady Navier -Stokes Equations are solved on spatial grids that are sufficiently fine, enable to resolve the Kolmogorov length scales at which energy dissipation takes place with time steps sufficiently small to resolve the period of the fastest fluctuation. This approach is computationally prohibitive and not practical for the industrial flows hence, it is not considered for practical reasons (Versteeg and Malasekera, 2007)

3.2.2   Large eddy simulation (LES)

Large Eddy Simulation is regarded as the intermediate form of turbulence calculations which tracks the behaviour of large eddies. The method involves space filtering of the unsteady Navier-Stokes equations prior to the computations, which captures the larger eddies and reject the smaller eddies. The effects on the resolved mean flow, plus large eddies due to the smallest unresolved eddies are included by means of sub-grid scale model. Since the unsteady flow must be solved then the demand on the computation resources and storage becomes enormous (Versteeg and Malasekera, 2007). Although this technique is starting to address CFD problems when dealing with complex geometries, it still beyond the limit of resources available for a basic CFD study.

3.2.3   Reynolds Average Navier-Stokes Simulation (RANS)

Reynolds Average Navier -Stokes approach to turbulence modelling is focused on the mean flow and the effects of turbulence on the mean flow properties. Prior to the application of numerical methods, the Navier-Stokes equations are time averaged. The extra term that appear in the time averaged flow equations is due to the interactions between various turbulent fluctuations and they are modelled with classical turbulent models e.g. k-Ɛ models and Reynolds stress model. (Versteeg and Malasekera, 2007)

This approach is widely used for most industrial flows and since in practice, underwater gliders operates at very low speeds ranging from 0.25m/s to 0.5m/s, at the corresponding Reynolds number of between 1×10^5 to 1×10^6; Zhang et al.;(2013), RANS equation becomes readily application in this situation. (Jagadeesh et al., 2009), recommends the use low Reynolds turbulence models such as the RANS equation for incompressible flow as proposed by (Javaid et al., 2017) when dealing with underwater gliders. The classical eddy-viscosity turbulence models are used to resolve the turbulence terms in Reynolds Averaged Navier-Stokes equations.

3.3 TURBULENT FLOW

In general, flow over external bodies is considered turbulent when the Reynolds number is greater than (Re>5x10^5). Turbulent could be thought as instability to the laminar flow at high Reynolds numbers (Re). These instabilities origin form interaction between non-linear inertial terms and viscous terms in Navier-Stokes equation. The nature of these interactions is rotational, fully time dependent and three dimensional as shown in figure 3.1. In true essence, rotational and three-dimensional interactions are connected through vortex stretching. It is almost impossible to obtain vortex stretching in two-dimensional space, hence most satisfactory approximations are three dimensional.
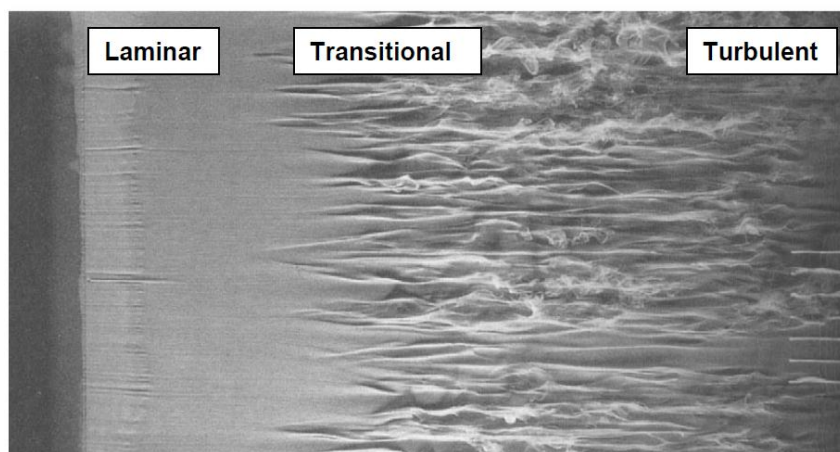
Figure 3-1 Growth of turbulent spots in a flat plate boundary layer(Nichols, n.d.)

Since this study focus on underwater gliders, the dimensions and velocities of typical underwater gliders are such that the Reynolds number is greater than 1.0 x10^6 which falls within the low turbulent flow regime as given in equation 2.1.

The initial speed of the underwater glider given as 0.1 m/s and the theoretical calculation showed that underwater gliders due to the nature of their speed they operate at low turbulent zone. Numerically turbulent flow simulation equations are solved for a time-independent velocity field that represents the velocity field $U(x,t)$ (Anon ,2000:362).

3.3.1 Turbulence modelling

Three two-equation models' predictions of the hydrodynamics and flow field are compared to see the model that can closely predict the physics of the problem. The models used are k-ε model (Standard), k-ε model (RNG) and k-ε model (Realizable). The k-term focuses on the mechanisms that affect the turbulent kinetic energy whereas ε-term focuses on turbulent dissipation rate. The instantaneous kinetic energy of a turbulent flow is then given by the sum of the mean kinetic energy as shown in equation 8.(Versteeg and Malasekera, 2007)

$$k(t) = K + k \tag{3.8}$$

where $K(t) = \frac{1}{2}(U^2 + V^2 + W^2)$ and $k = \frac{1}{2}\left(\overline{u'^2} + \overline{v'^2} + \overline{w'^2}\right)$

The governing equation for mean flow kinetic energy k can be written as shown in equation (3.9)

$$\frac{\partial(\rho K)}{\partial t} + \text{div}(\rho K \mathbf{U}) = \text{div}\left(-P\mathbf{U} + 2\mu \mathbf{U} S_{ij} - \rho \mathbf{U}\overline{u_i' u_j'}\right) - 2\mu S_{ij}.S_{ij} + \rho\overline{u_i' u_j'}.S_{ij} \tag{3.9}$$

The governing equation for the turbulent kinetic energy k is given by equation 10

$$\frac{\partial(\rho K)}{\partial t} + \text{div}(\rho K \mathbf{U}) = \text{div}\left(-\overline{p'\mathbf{u}'} + 2\mu\overline{\mathbf{u}'s'}_{ij} - \rho\frac{1}{2}\overline{\mathbf{u}_i'.u_i' u_j'}\right) - 2\mu\overline{S'_{ij}.S'_{ij}} - \rho\overline{u_i' u_j'}.S_{ij} \tag{3.10}$$

The k-ε model uses the following transport equations for k and ε given in equation (3.11) and (3.12) respectively.

$$\frac{\partial(\rho K)}{\partial t} + \text{div}(\rho K \mathbf{U}) = \text{div}\left[\frac{\mu_t}{\sigma_k} grad k\right] + 2\mu S_i.S_{ij} - \rho\varepsilon \tag{3.11}$$

where $\mu_t = \rho C_\mu \frac{k^2}{\varepsilon}$

$$\frac{\partial(\rho\varepsilon)}{\partial t} + \text{div}(\rho\varepsilon \mathbf{U}) = \text{div}\left[\frac{\mu_t}{\sigma_\varepsilon} grad\varepsilon\right] + C_{1\varepsilon}\frac{\varepsilon}{k}2\mu_t S_{ij}.S_{ij} - C_{2\varepsilon}\rho\frac{\varepsilon^2}{k} \tag{3.12}$$

Since this study used k-ε(RNG) model, the equations for k and ε for the model is given by equation (3.13) and equation (3.14) respectively.

$$\frac{\partial(\rho\varepsilon)}{\partial t} + \text{div}(\rho K \mathbf{U}) = \text{div}\left[\propto_k \mu_{eff} grad\ k\right] + \tau_{ij}.S_{ij} - \rho\varepsilon \tag{3.13}$$

$$\frac{\partial(\rho K)}{\partial t} + \text{div}(\rho\varepsilon \mathbf{U}) = \text{div}\left[\propto_\varepsilon \mu_{eff} grad\ \varepsilon\right] + C_{1\varepsilon}^*\frac{\varepsilon}{k}\tau_{ij}.S_{ij} - C_{2\varepsilon}\rho\frac{\varepsilon^2}{k} \tag{3.14}$$

where $\tau_{ij} = -\rho\overline{u_i' u_j'} = 2\mu_t S_{ij} - \frac{2}{3}\rho k\delta_{ij}$ and $\mu_{eff} = \mu + \mu_t$

$C_\mu = 0.0845$ $\alpha_k = \alpha_\varepsilon = 1.39$ $C_{1\varepsilon} = 1.42$ $c_{2\varepsilon} = 1.68$

3.4   NUMERICAL METHOD

Numerical solution is obtained following different numerical steps as discussed below.

3.4.1   Computational domain

The computational fluid domain is described as the boundary or a fluid zone that depicts a real-life scenario or environment of the problem. Usually the target object of interest is placed inside the domain positioned categorically by following guidelines as detailed in section 5.3. The computational fluid domain can be created in many ways depending on the choice of the end user. In this study, the computational fluid domain is created using a proprietary CAD software (Solidworks 2017, Dassault Systemes), then imported to ANSYS work bench 18.1. The next step was the discretisation of the computational fluid domain referred to as meshing.

3.4.2   Mesh (general overview)

In numerical approach, one has to define the problem in a manner that is easy to compute by looking at the surfaces, boundaries, spaces around the computational domain and break it down into small infinitesimal cells or elements. This process is termed meshing or discretisation. In general, as shown in figure 3.5 there are three major aspects of discretisation when solving fluid flow problems namely: Equation discretisation, Spatial discretisation and Temporal discretisation.
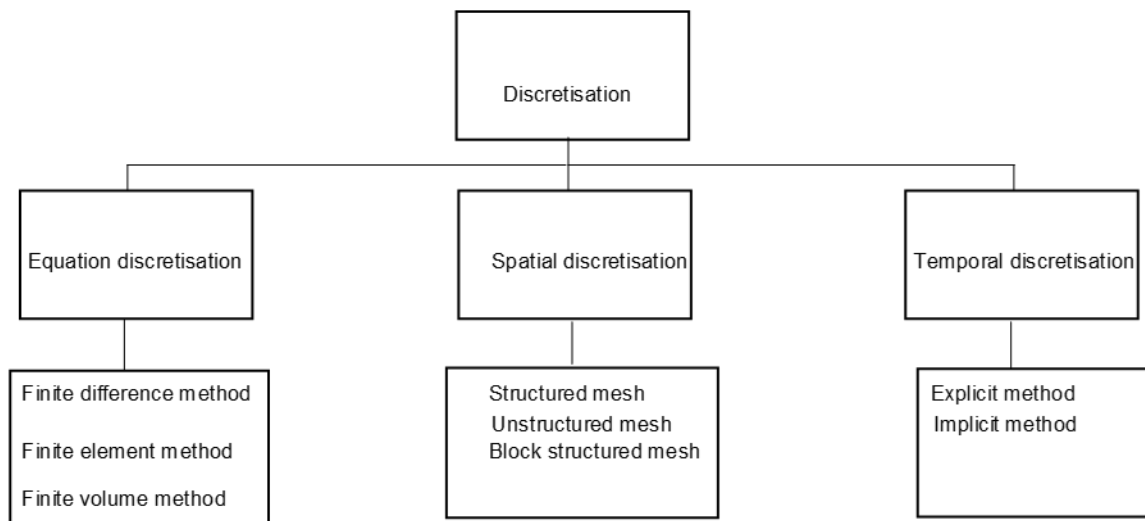

Figure 3-2 Discretisation of flow in CFD

3.4.2.1 Equation discretisation

Equation discretisation is carried out in numerical simulation using three methods: finite difference method (FDM), finite element method (FEM) and Finite volume method (FVM).

3.4.2.1.1 Finite difference method

Finite difference methods apply Taylor expansion method to solve second partial differential equations (PDEs) of the governing equation for fluid flow. The method arranges the derivatives of the PDEs and write them in discrete quantities of variables yielding simultaneous algebraic equations, with unknowns defined at the nodes of the mesh. FDM gained its popularity due to its simplicity and ease in obtaining higher order accuracy discretisation. However, FDM has limitation such that it can only be applied on simple geometries as it requires structured mesh.

3.4.2.1.2 Finite element method

Finite element method has the ability to solve complex geometries as it employs unstructured mesh, where a computational domain is divided into finite number of elements and within each element, a certain number of nodes are defined and the numerical values of the unknown are determined. In finite element method, the discretisation is obtained using the method of weighted residuals, that approximate the solution to a set of partial differential equations using interpolation functions. However, this method requires high computing power compared to the finite difference method

3.4.2.1.3 Finite volume method

This method integrates the governing equations for fluid flow and solve them iteratively based on the conservation law on each control volume. This discretisation process results in a set of algebraic equations that solves the variables at a specified finite number of points within the control volumes, which then the flow around the domain can be modelled. This method can employ structured and unstructured mesh. Since this method uses direct integration, it is more efficient and easier to program in terms of CFD code development. This method uses less

computing power whereas it can solve simple and complex geometries and is more common in recent CFD applications compared to FEM and FDM.

3.4.2.2 Spatial discretisation

Spatial discretisation divides the computational domain into small sub domain making up the mesh. This defines each subdomain mathematically specifying its velocity at all points in space and time. There are three different mesh types mainly used in CFD namely: structured, unstructured and multi-block structured mesh. Structured mesh is built on a coordinate system, commonly used in simple geometries such as square and rectangular. The structured mesh performs badly when applied to complex geometries hence switch to the unstructured mesh when dealing with complex geometries.

Unstructured mesh gives the allowance to rearrange elements and nodes on the computational domain such that different kinds of complex geometries can be simulated. In as much unstructured mesh works well with complex geometries it comes at a cost, as it requires more computing power. In order to compensate for computing cost and flexibility, multi-block structured or hybrid mesh is then deployed. Multi-block structured mesh generates a mesh that consist of structured and unstructured mesh. However, it is very complicated to generate a multi-block structured mesh as oppose to the structured mesh, but the multi-block structured mesh gives control to refine sharp edges, corners and surfaces with suitable mesh type, based on the complexity of the geometry.

3.4.2.3 Temporal discretisation

Temporal discretisation works with time, whereby it divides the time in a continuous flow into discrete time steps. Transient or time dependent formulations, comprise of an additional time variable t in the governing equations compared to the steady state analysis. This then leads to a system of partial differential equations in time, which comprise of unknowns at a given time as a function of the variables of the previous time step. Hence, unsteady simulation requires longer computational time compared to a steady case due to the additional steps between the equation and spatial discretisation.

3.5 SOLUTION METHODS

ANSYS Fluent have two solution methods available, pressure velocity-coupling and density-based. Pressure velocity-coupling solves pressure and velocity simultaneously whereas density-based method implements segregated approach where each variable pressure and velocity are solved in series of time. In this study since we are solving for pressure and velocity therefore pressure-velocity coupling method is used in this study.

3.6 HYDRODYNAMIC FORCES

In practice, it is always difficult to move a body through a fluid due to the resistance the fluid to the motion of the body immersed in it and this phenomenon is called drag. It is important to note that a stationary fluid exert only normal pressure forces on the surface of the submerged body whereas a moving fluid exerts tangential shear forces on the surface because of no-slip condition caused by viscous effects. This effect constitutes the basic hydrodynamic interactions between a moving body and the fluid. Other interactions such as buoyancy and gravitational forces are negligible and therefore not considered in this work. Both forces in general have components in the direction of the stream flow thus drag force is regarded as the combination of the effect of pressure and wall shear forces in the direction of the flow.(Cimbala and Cengel, 2009)

These components are termed skin friction drag (due to shear forces on the surface) and form drag (due to pressure normal to the flow direction acting in the frontal or projected area) as shown in equation (3.15).

$$F_D = C_D A \frac{\rho V^2}{2} \qquad (3.15)$$

where C_D is the coefficient of drag, A the projected area, ρ density of the fluid and V free stream flow velocity of the fluid.

The Lift force is considered as the components of the pressure and wall shear forces in the normal direction but opposite gravitational force and is given by equation (3.16).

$$F_L = C_L A \frac{\rho V^2}{2} \qquad (3.16)$$

Where C_L is the coefficient of Lift, A is the area normal to the force ρ density of the fluid and V stream flow speed of the fluid.

Surface pressure coefficient due to static pressure acting normal to the glider wing is given by equation (3.17).

$$C_P = \frac{P_i - P_\infty}{\frac{1}{2}\rho V^2}$$
(3.17)

Where P_i is the surface static pressure

CHAPTER 4

COMPUTATIONAL FLUID DYNAMIC SETUP

4.1   GLIDER GEOMETRIC DESIGN

Several standard aerofoil shapes are frequently used in aerodynamic and hydrodynamic designs. The most popular is the NACA aerofoil standard (Abbott, n.d.). In this study, a standard NACA 0016 chosen after preliminary geometric designs considerations was modified and evaluated. A numerical simulation was thereafter performed to evaluate the hydrodynamics of the modified version of the NACA wing.

A computational model was developed to investigate the hydrodynamic behaviour of the modified standalone NACA wing as opposed to the one that is attached on the fuselage of the underwater glider under turbulent hydrodynamic conditions. The following tasks was carried out in performing the analysis. This include geometry creation, computational mesh generation, numerical solution and post processing.

(a)   (b)
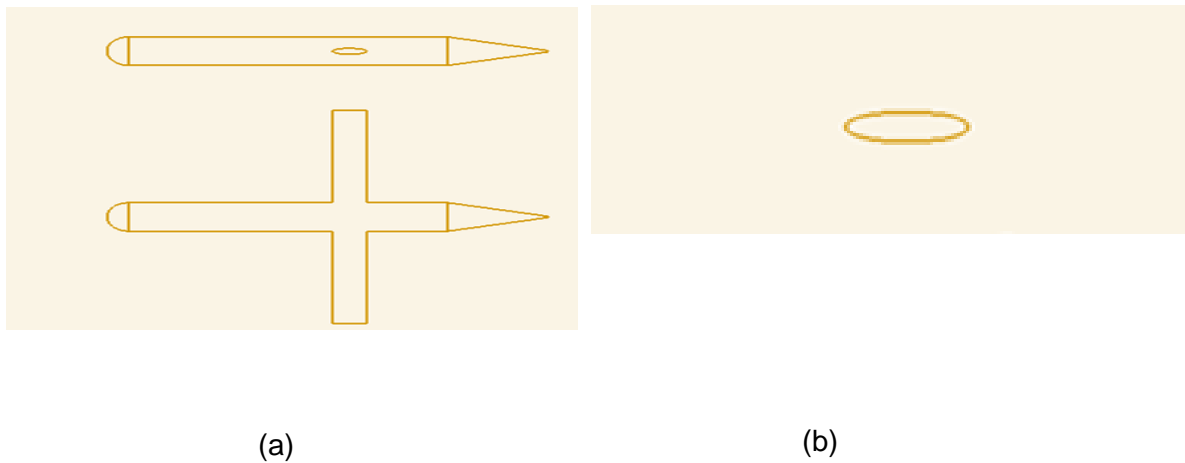
Figure 4-1 Schematic illustration of the glider and the adapted/modified NACA wing (a) Glider model (b) Modified NACA 0016 wing

4.1.1   Flow domain creation

Online NACA wing geometry point generator was used to download NACA0016, 2D aerofoil geometry points. The geometry points are saved into a notepad then imported to Computer aided draughting CAD software (Solidworks,2017) as shown in Table 4.1.

Table 4-1 Truncated geometry points of the overall NACA0016

Points	X	Y	Z
1	1mm	0mm	0mm
2	1mm	0mm	0mm
3	0.99mm	0mm	0mm
4	0.99mm	0mm	0mm
5	0.98mm	0mm	0mm
6	0.96mm	0.01mm	0mm

a

b
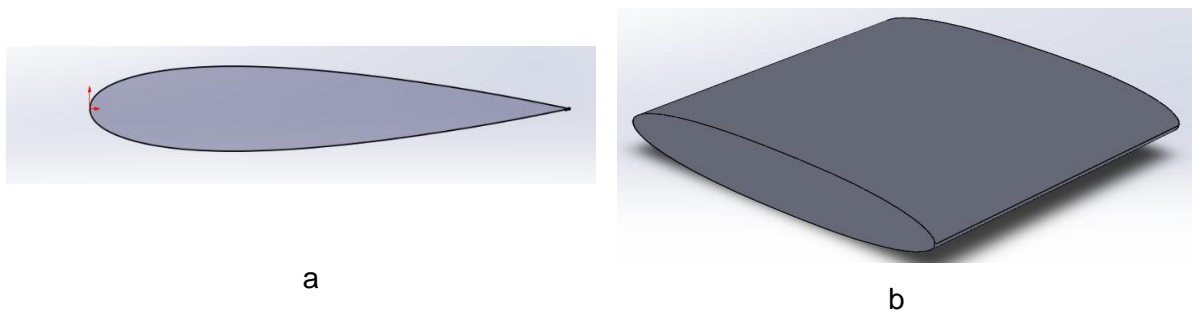
Figure 4-2 2D scaled NACA0016 airfoil and modified CAD 3D wing

Figure 4.1 (a) shows a 2D model of the NACA0016 aerofoil. Using Solidworks CAD tools, the 2D model is modified further and converted into a 3D model as shown in (b). The overall summary of the dimensions of the glider wing are shown in Table 4.2.

Table 4-2 Dimension of the glider wing

Dimensions	Round trailing edge wing
Total wing span	300 mm
Root Chord Length	170 mm
Diameter of the wing	45 mm
Taper Ratio	-
Sweep Angle	90 degrees

The fluid domain is created following the guidelines of (Javaid et al., 2016). The ITTC guidelines (Bertram, 2012) state an upstream boundary 1-2 times the length of the glider, and the downstream boundary 3-5 times the length of the glider. (Zhang et al., 2013) and (Javaid et al., 2016) conducted similar investigation on submerged bodies, with similar boundary parameters, where the inlet flow was set to be 1.5 times the length of the glider and 3.5 times away from the glider.

The ceiling and bottom wall were given as 9 times the diameter of the glider to avoid the error effect caused by an interruption in the fluid flow. The solution domain for this work followed the approach of (Javaid et al., 2017). The dimensions of the fluid domain are as follows: upstream boundary is set at 2 times the length of the glider wing; downstream boundary is 4 times the length of the glider wing and from the ceiling-wall of the domain to the wing plane and from the bottom wall domain to the wing plane is 9 times the glider wing diameter as shown in figure 4.3.
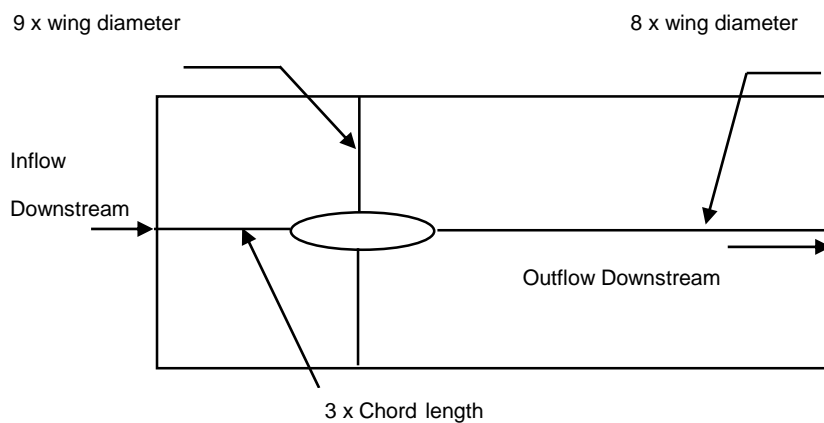

Figure 4-3 Computational Dimensions

4.1.2   Computational mesh

Multizone is selected as the method to generate the mesh. Since the multizone generate structured mesh as shown in figure 4.4, it was then easy to obtain an acceptable mesh metrics in terms of the orthogonal mesh quality and skewness ratio.
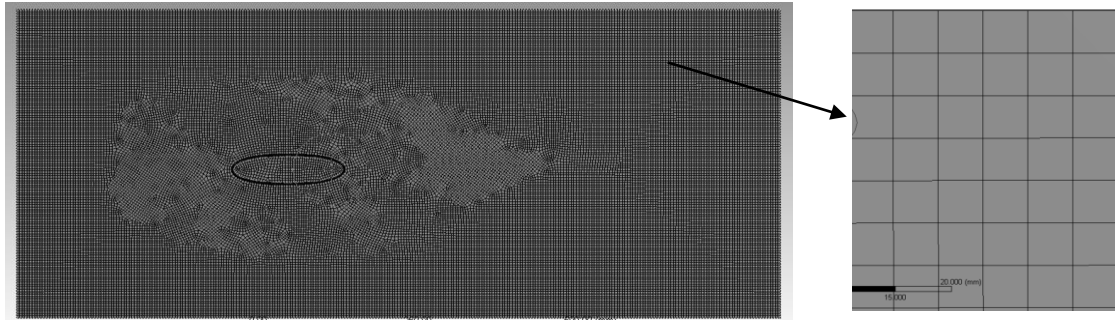
Figure 4-4 Computational domain mesh

In areas where the geometry contains high curvature, Multizone employed unstructured mesh which captures the full details of the geometry as shown in figure 4.5. A summary of the mesh metrics of the study is given in table 4.3.
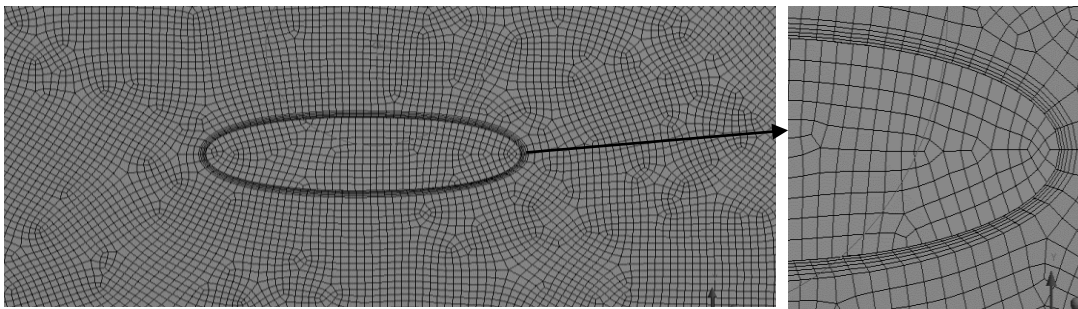

Figure 4-5 Closer view mesh around the modified glider wing

Table 4-3 Summary of the grid generation

Mesh generation and Quality					
Mesh Method	Mesh density	Computational time	Aspect ratio	Skewness	Orthogonal Quality
Multizone	635,256	2hrs/per1000 iteration	1	1.5072e-005	0.62

4.1.2.1 Theoretical considerations

The primary lifting surface of the glider is the wing. If the wing is sliced in many sections along the span is called an aerofoil or in this study since we are dealing with water is called hydrofoil.(Anon, n.d.).The hydrofoil can be taken as an infinitely long 2D wing that has the same cross sectional shape. In principle, if the hydrofoil moves near the surface of the water, it will experience resistance due to many factors such as the wave making drag caused by boundary vortices in proximity to the surface, induced drag caused by trailing vortices and profile drag caused by frictional and eddy making drag. The wing since is 3D is treated and

29

finite wing and usually the in the aerofoil, the wing coefficient of lift and drag are denoted by C_L and C_D, whereas for hydrofoils these are denoted by C_l and C_d with lower case to distinguish the two.

In the case of shallow water application, there is a maximum velocity which is due to the propagation of waves called critical velocity. If the semi-submerged object moves at super critical speed, the wave caused by bound vortices does not follow which results in no wave making drag. A deeply submerged hydrofoil act as an aerofoil in infinite medium therefore the effect of the free surface is negligible.

The principle of the physics around the aerofoil and hydrofoil is the same as the difference is the fluid medium. The air deals with compressible flow whereas water and ideal gas deals with incompressible flow. The hydrofoil moves through the water and experience the hydrodynamic force which is divided into two components called the drag and lift force.

The lift force is defined as the force acting normal to the surface area of the hydrofoil, whereas the drag is the force acting parallel to hydrofoil surface. These two components are a function of the angle of attack (AOA), free stream velocity and submergence depth. The hydrofoil with infinite span generates only profile drag and section drag due to the absence of induced drag and induce downwash angle. However, in the case of finite wing span, the induce drag and induce downwash angle must be taken into consideration and figure 4.6 shows typical curve of wing characteristics.
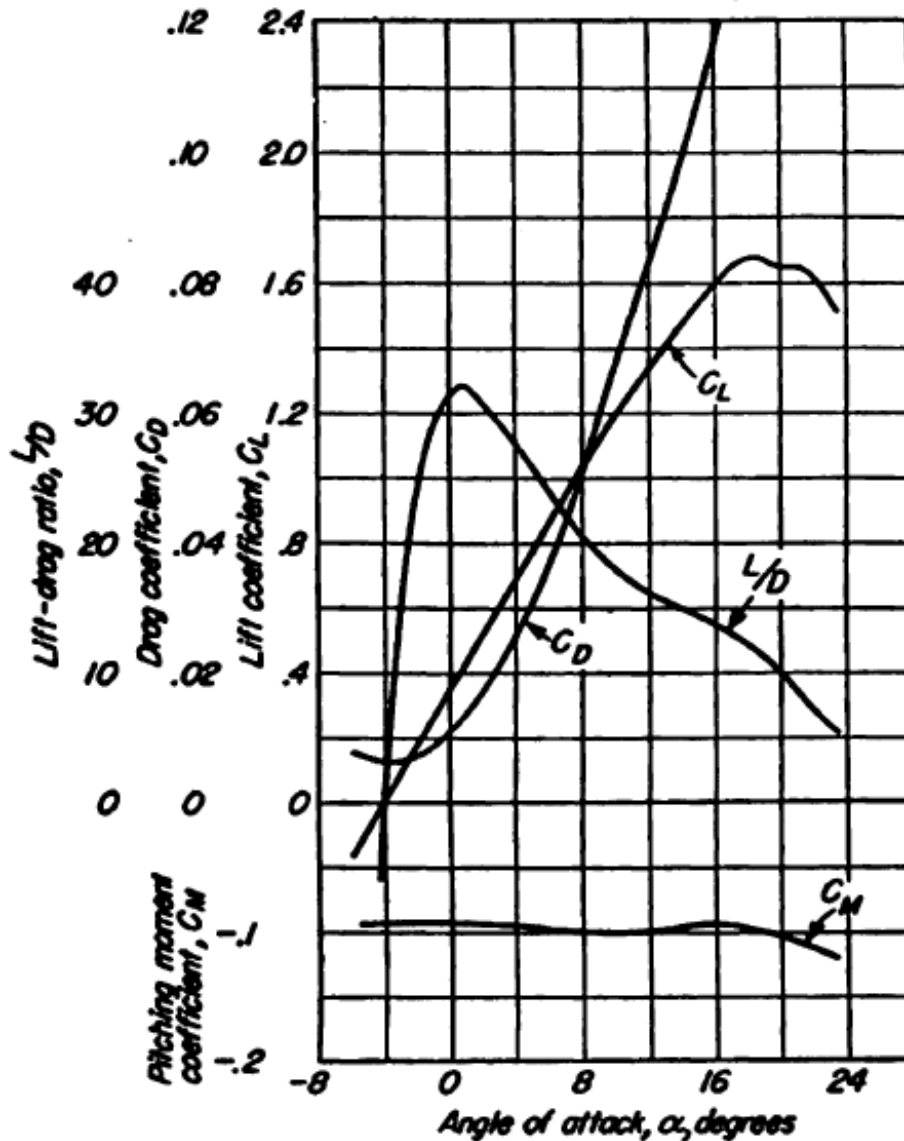
Figure 4-6 Typical wing characteristics (Abbott, n.d.)

In this work, steady-state CFD analysis were performed to determine the hydrodynamic characteristics of the underwater glider wing. The motion of the fluid is modelled using ANSYS Fluent 18.1using the incompressible form of Reynolds Averaged Navier Stokes (RANS) equation to determine the flow field and the pressure around the glider wing.

Javaid and his team (Javaid et al., 2016), reports that different turbulence models are used to date to resolve Reynolds stress tensor to determine the unknown values. Since in nature, underwater gliders operates at very low speeds ranging from 0.25m/s to 0.5m/s, at the corresponding Reynolds number of between 1 x 10^5 to 1 x 10^6 ;(Zhang et al., 2013) when carrying out an investigation on this type of vehicle as well as (Jagadeesh et al., 2009) recommends the use of low Reynolds turbulence models. Therefore, based on this recommendation, the three classical k-ℇ turbulence models were chosen for this study and

31

their predictions are compared to determine the one that yield reasonable result matching or close to the published experimental data.

4.1.2.2 Turbulence resolution

According to (Javaid et al., 2016), underwater gliders operate within the speed range of 0.25m/s to 0.5 m/s, resulting in the Reynolds range of 1×10^5 to 1×10^6, which is classified as low turbulence region. A steady-state analysis was employed to calculate the hydrodynamic forces of the external flow on underwater glider wing. The selection of the CFD approach for this study was compared with what is currently used by researchers and industrial partners versus viable computational cost and for these reasons, Reynolds Averaged Navier-Stokes (RANS) approach proved to be the most widely used and cost-effective approach. The RANS turbulence models are divided into zero equation model, one equation model, two equations and seven equation models. The study only focusses on the three k-epsilon two equation models which solves turbulent kinetic energy equation k and turbulent dissipation ε. The three k-epsilon models include Standard, Re-normalization group (RNG) and Realizable group and their equations are discussed in detail in section 3.1.

The study investigated how the geometric design variations and operational parameters, (AOA, speed and chord length) influence the hydrodynamic parameters (pressure, velocity, drag coefficient, lift coefficient and pressure coefficient). Table 4.6 shows the ranges of the speed and Reynolds numbers used in carrying out the study while the software-specific settings are shown in table 4.5.

Table 4-4 Theoretical values of the flow quantities at different operating speeds and Reynolds range

	1st	2nd	3rd	4th	5th	6th
Velocity(m/s)	0.1	0.26	0.28	0.3	0.4	0.5
Reynolds number	10663.4	27725	29857.7	31990.3	42653.8	53317.2

The formula for calculating Reynolds number is given by equation 4.1 as:

$$Re = \frac{\rho v Dh}{\mu}$$
(4.1)

Where ρ is the density of the fluid, v velocity of the stream flow, Dh hydraulic diameter of the wing which is given by equation 4.2 and μ kinematic viscosity of the fluid.

$$Dh = \frac{a.b}{\sqrt{\frac{a^2+b^2}{2}}}$$

(4.2)

Where a is the thickness of the wing and b is the chord length.

4.1.3   Numerical solution strategy and control

The convergence criterion is used to verify the accuracy of the numerical simulation by monitoring the following parameters while computing the numerical solution: residual plots, drag and lift coefficient s. The residual monitors satisfy convergence criterion when the continuity, velocity (X, Y, Z), epsilon and k, drops below (1.0×10^{-4}) as shown in figure 4.13 (Canonsburg, 2017). The number of iterations for running the simulation was set to at least 1000 iterations to ensure full convergence of the numerical results.
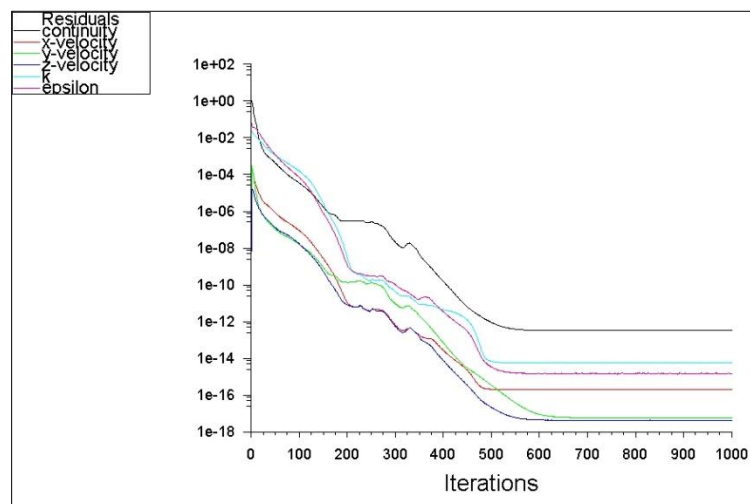

Figure 4-7 Convergence monitor using residuals curves

The solution control parameters such as the relaxation and under-relaxation control factors shown in table 4.6 were used to control the stability of the numerical computations.

4.1.3.1 Solution parameters in fluent

The solution of the flow field representing incompressible fluid under steady state condition is achieved by solving the Navier-Stokes equations using RANS approach. These equations are discretized using finite volume approach. The solver settings implemented are double

33

Table 4-5 Control parameters -Relaxation and Under-Relaxation factors

Control Parameter	Relaxation factors
Flow courant number	200
Momentum	0.5
Pressure	0.5
Control Parameter	Under- Relaxation factors
Density	1
Body forces	1
Turbulent Kinetic energy	0.75
Turbulent dissipation rate	0.75
Turbulent viscosity	1

precision and pressure-based solver. Second order upwind scheme is used to approximate the momentum equations, whilst the pressure-velocity coupling is realized through the couple method. The boundary conditions and assumptions for correctly solving the physics of the problem are discussed in section 4.6.1 and Table 6 gives a summary of the overall solution approach.

4.1.3.2 BOUNDARY CONDITIONS

The boundary conditions for the computational domain are illustrated in figure 4.9. The flow enters the computational domain from the upstream side with a free stream velocity of 0.26m/s (Velocity -Inlet) and exit the computational domain downstream with atmospheric pressure (pressure outlet). The flow is bounded by the walls (Ceiling, Bottom and back walls) with a standard no-slip condition which implies that the velocity increases from zero at the wall surface and to the free stream velocity away from the surface. To reduce the computational load, a symmetry boundary condition is used at the symmetric plane where the conditions are set to zero.
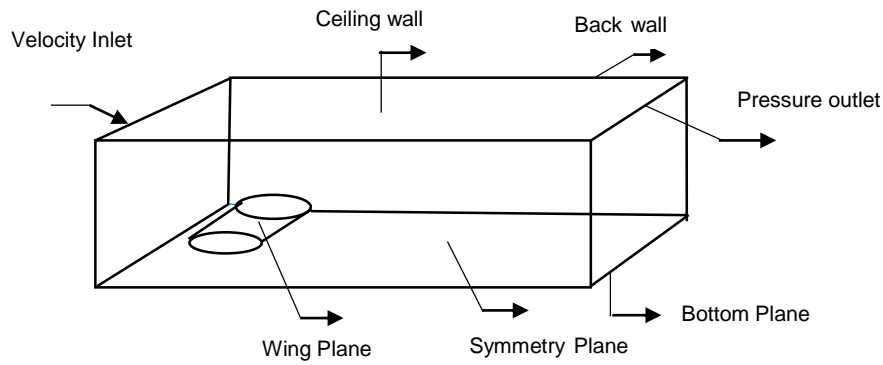
Figure 4-8 Computational Domain boundary conditions

Table 4-6 Summary of the numerical simulation parameters in ANSYS Fluent

Settings	Choice
Simulation type	3D Steady state
Solver	Double precision, Pressure based
Temporal discretization	Second order
Turbulent model	K-epsilon (RNG), Realizable and Standard
Pressure -velocity coupling	Couple
Momentum	2nd order upwind
Volume fraction	2nd order upwind
Turbulent kinetic energy	2nd order upwind
Turbulent dissipation rate	2nd order upwind
Convergence criterion	1.0×10^{-4}

4.1.3.3 Resolution of the near wall effect

In external flow simulation, the fluid behaviour away from the boundary layer can easily be estimated due to its uniformity but closer to the wall, the fluid behaviour is unpredictable. Near wall treatment is often employed in CFD to resolve the behaviour of the flow near an obstacle or a wall. There are techniques implemented in this work to a certain degree to minimize the CFD error due to the influence of this effect. For instance, inflation layers were used to capture the turbulent effect around the wing and finer mesh around the wing was used to resolve the finer details of the flow behaviour close to this surface. In addition, this study also employed the built-in capability of the two equation turbulence models in ANSYS Fluent for handling the near wall effects. These capabilities range from: Standard Wall Functions, Scalable Wall Functions, Non-Equilibrium Wall Functions, Enhance Wall Treatment (EWT), Menter-Lechner and User Defined Wall Functions.

4.1.3.4 Mesh sensitivity test

In ensuring that we have proper control over the numerical solution strategy, our chosen fluid flow equation and applied boundary condition must be solved correctly. This is achieved by performing a mesh sensitivity analysis to ensure our numerical solution is grid-independent. The residuals levels were used to gauge the accuracy of the simulation and also lift and drag coefficients to monitor convergence. However, in the present work the grid convergence analysis is deemed sufficient for the solution control.

In the performing the mesh sensitivity test, the CAD geometry was transferred into ANSYS mesh to create the computational grid. Four grids were created with the following densities: 56,360; 312,796; 635,256 and 899,000. The test with varying mesh densities is carried out to satisfy grid independence to determine an optimum mesh or grid size to be employed for further numerical computations. Figure 4.2 shows the velocity profiles for different mesh densities. It is observed that a mesh of 635,256 cells exhibits no further improvement in terms of the numerical results and it is then selected to carry out the numerical investigation.
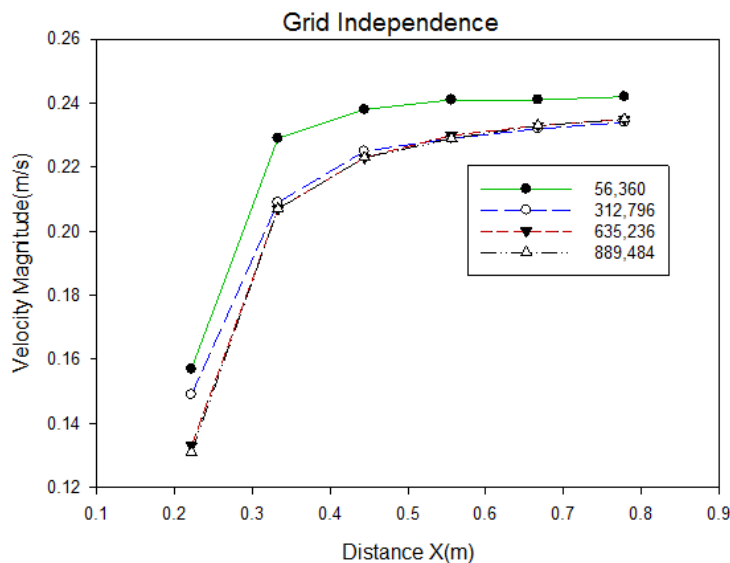

Figure 4-9 Velocity profile of modified NACA0016 wing for various mesh densities

CHAPTER 5

RESULTS AND DISCUSSION

The numerical results which are obtained from the CFD simulations following a CPU time of 3 hours for the optimized mesh density are post-processed and presented qualitatively and quantitively followed by a detailed discussion. The numerical simulation was performed on a MacBook Pro with the following specifications (RAM 16 GB, CPU Intel core i7 at clock speed of 2.7 GHz). The results are also compared with other published experimental data as a means of validation.

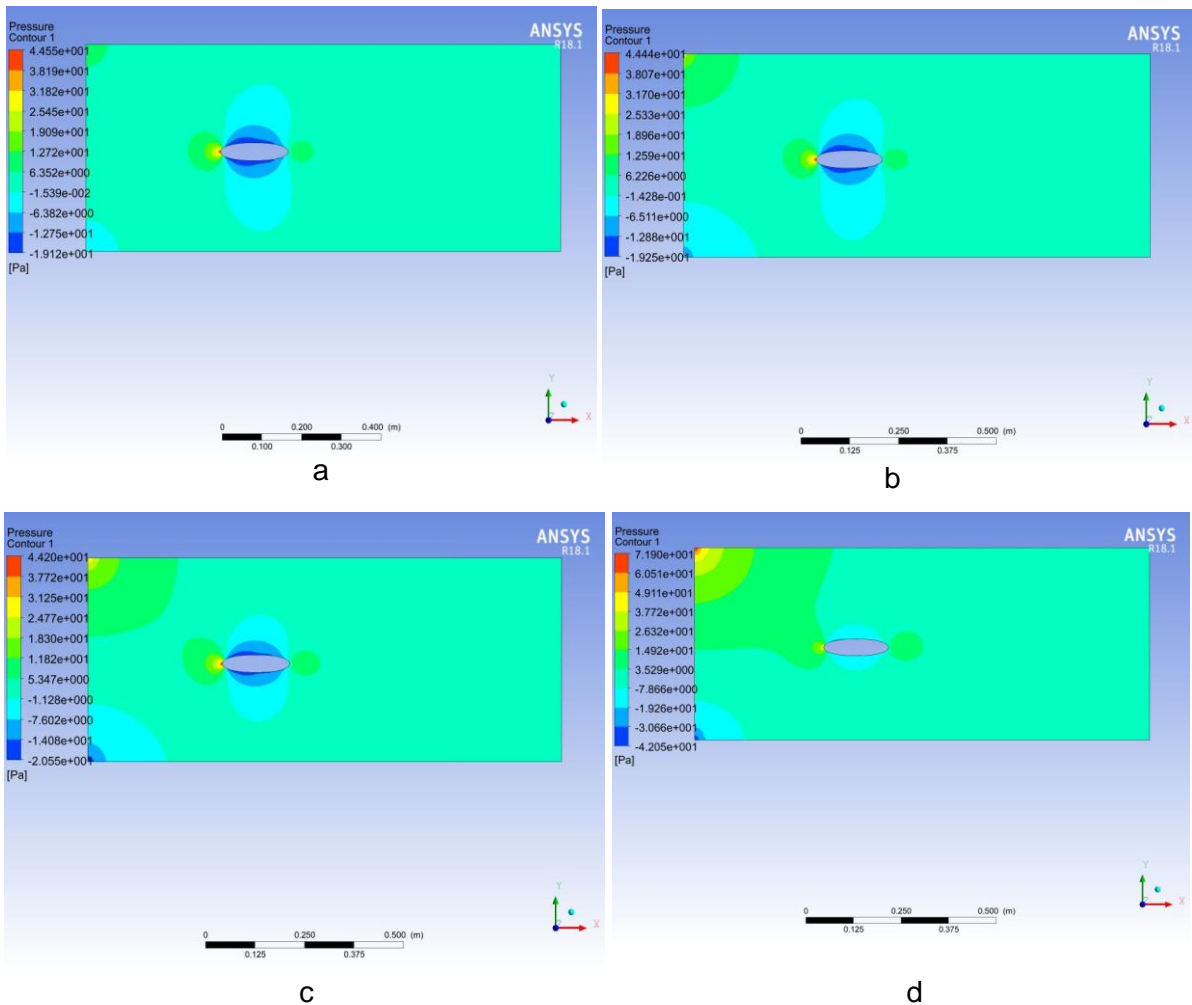## 5.1   QUALITATIVE DATA ANALYSIS
5.1.1   Pressure contour

Figure 5-1 Pressure contours along the YX plane at inlet velocity of 0.3m/s for K-Ɛ-RNG: (a) AOA=2 (b) AOA=4 (c) AOA=6 (d) AOA=14 at Z = 1mm.

Figure 5.1 shows YX plane contour plots for pressure distribution as a function of AOA from the inlet to the outlet of the domain at a free stream velocity of 0.3 m/s for k-Ɛ(RNG) model. It

is noticed that the pressure build-up is very high at the leading edge than any other section on the wing as expected as there is a lower pressure at the outlet. It is also noticed the pressure increase as the AOA increases. This then explains why the wing experience more drag at higher AOA than at lower AOA, whereas for the lift is the opposite.
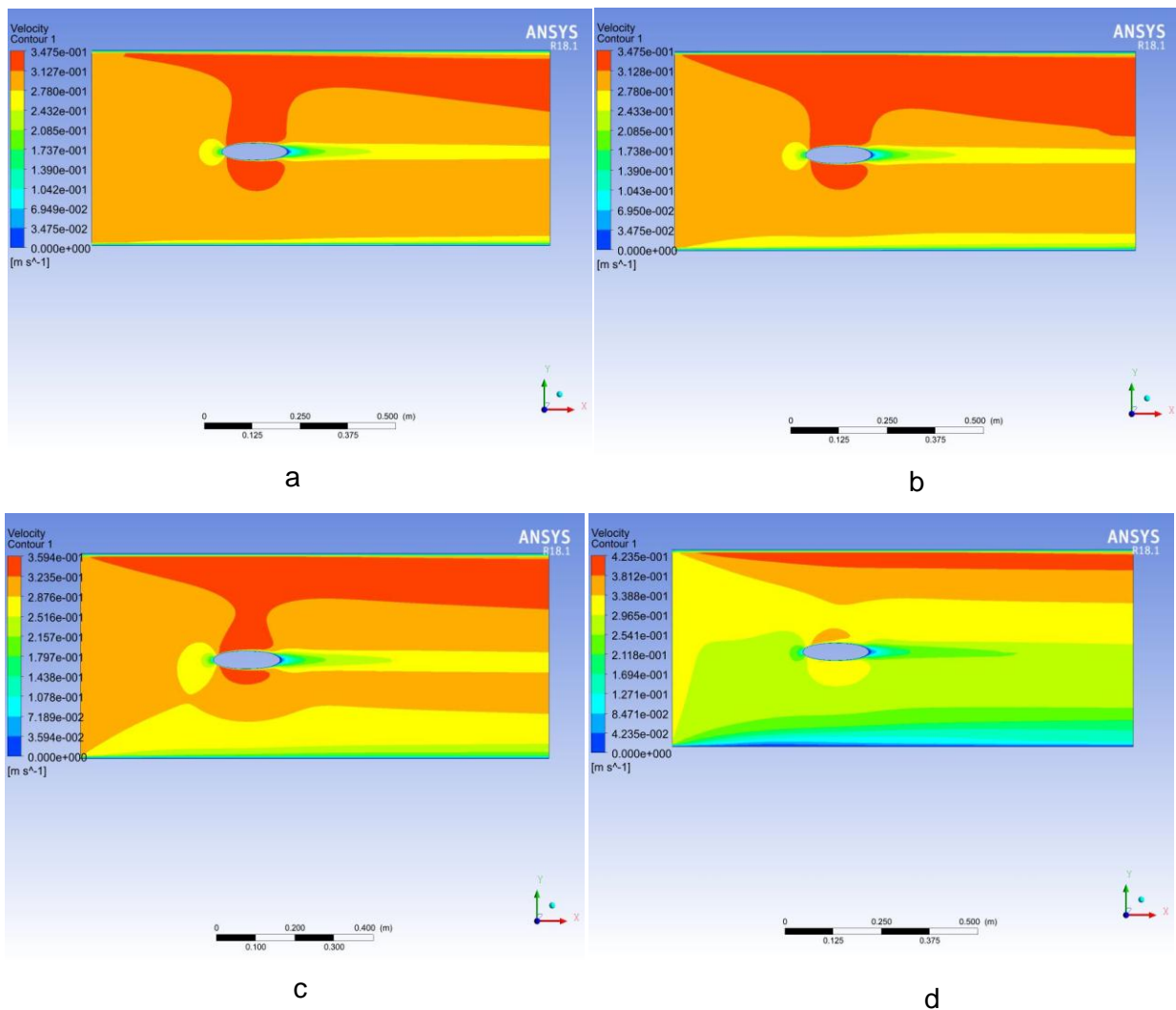
5.1.2   Velocity contour

Figure 5-2 Velocity contours along the YX plane at inlet velocity of 0.3 m/s for K-Ɛ- RNG: (a) AOA=2 (b) AOA=4 (c) AOA=6 (d) AOA=14 at Z = 1mm.

Figure 5.2 shows YX plane for velocity contours at Z = 1mm, with the constant free stream velocity of 0.3 m/s for k-Ɛ (RNG) for various AOA. It is observed the stream flow velocity is high at the upper surface of the wing than the bottom. This suggest as the AOA increases, the speed at the upper surface of the wing increases as well. The physical explanation for this

behaviour is the early separation of the fluid from the upper surface of the wing due to the increasing AOA giving fluid less contact area hence an increase in speed.
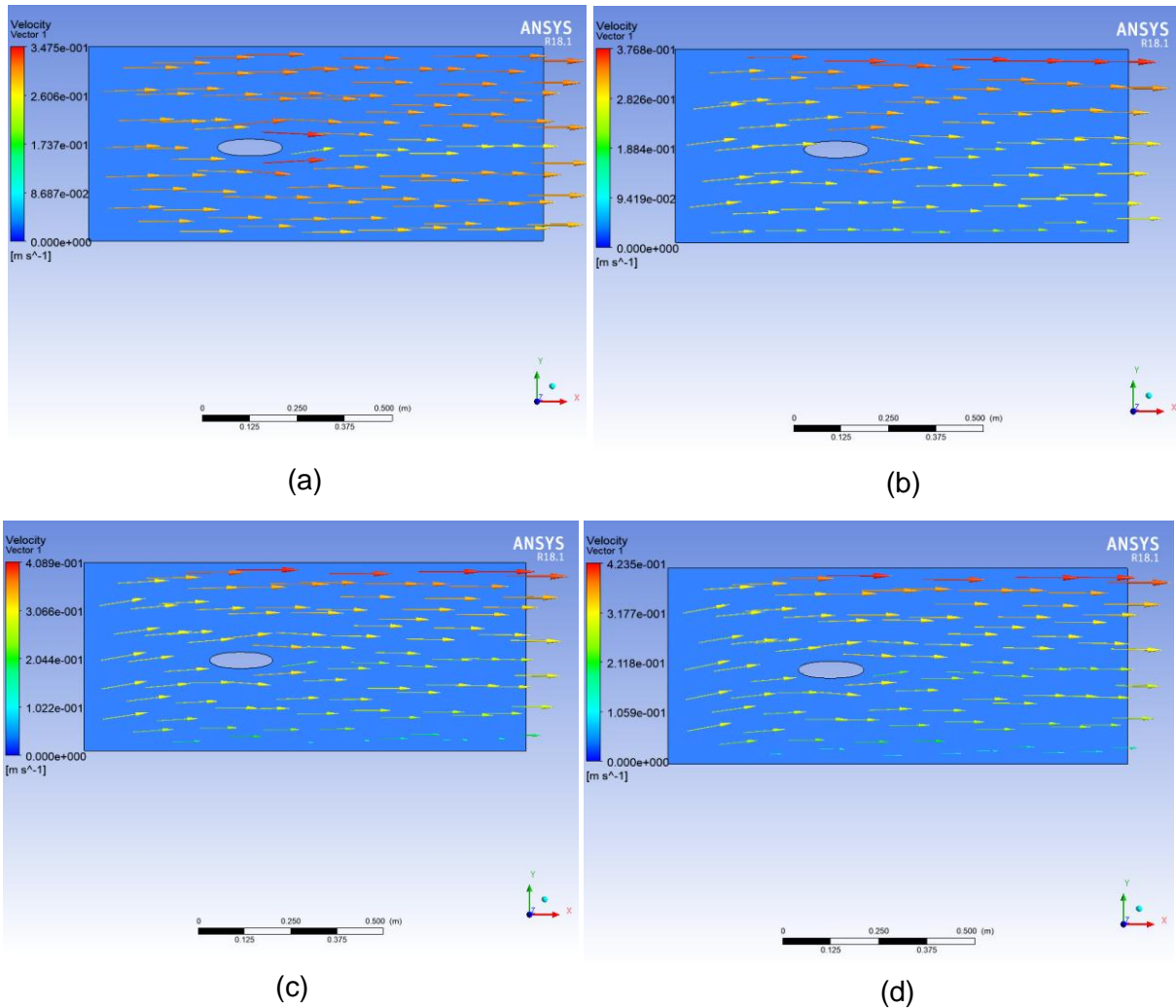
5.1.3 Velocity vectors

(a)   (b)

(c)   (d)

Figure 5-3 Velocity vectors along the YX plane at inlet velocity of 0.3m/s for K-Ɛ-RNG: (a) AOA=2 (b) AOA=4 (c) AOA=6 (d) AOA=14 at Z = 1mm.

Figure 5.3 shows velocity vector plots for various AOA, with a fixed velocity of 0.3 m/s for k-Ɛ (RNG). It is noticed that the fluid flow around the wing of the underwater glider agrees with the theoretical framework for external flow. As the AOA increases the fluid tends to follow the trajectory path of the wing as depicted by the figures (a) to figure (d). Figure 5.3 also agrees with figure 5.2 of the velocity contour as expected that the velocity increases with the AOA and is higher at the upper surface of the wing.
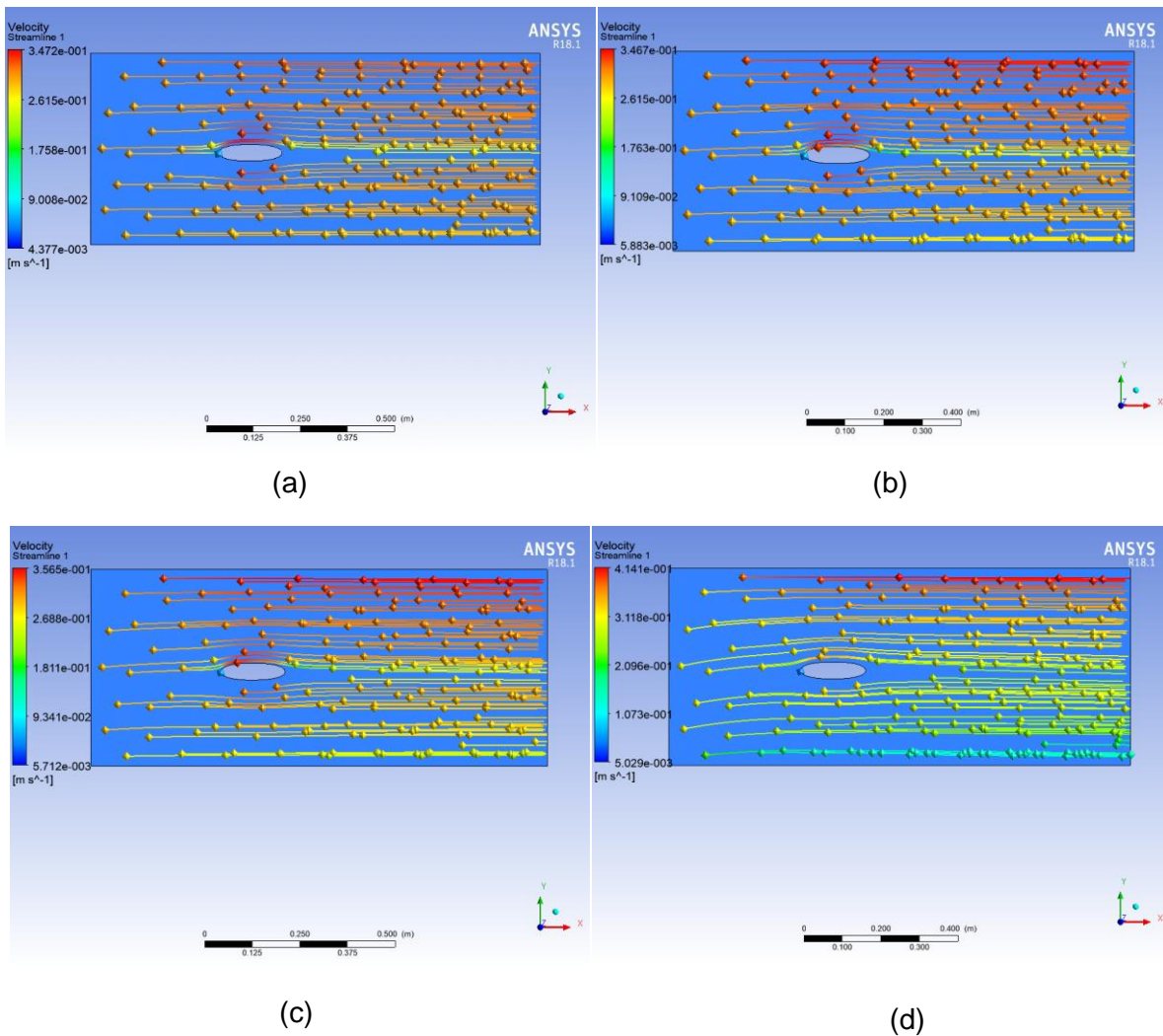
5.1.4   Velocity streamlines

(a)

(b)

(c)

(d)

Figure 5-4 Velocity streamlines along the YX plane at inlet velocity of 0.3m/s for K-Ɛ-RNG: (a) AOA=2 (b) AOA=4 (c) AOA=6 (d) AOA=14 at Z = 1mm.

Figure 5.4 shows the spatial representation of figure 5.3 and figure 5.2. The tracking of fluid particle streamlines with massless particles give a clear fluid flow path from the free stream inlet of the domain to the outlet in addition to depicting the variation of the flow velocities across the lower surface and the upper surface of the wing. We can also observe from the flow stream that the flow velocity magnitude shows a gradual decrease towards the pressure outlet.

5.2   QUANTITATIVE DATA ANALYSIS

The quantitative results of the spatial distribution of pressure, lift and drag coefficients along the upper and lower surface of the glider wing, (close to the fuselage, at the centre of the span and at the tip of the wing) are presented in the following sections. In comparing the influence of the operating conditions on the hydrodynamic performance, the numerical data were presented for different inlet velocities, angles of attack (AOA) and turbulence models. The selected operating conditions are as follows: inlet velocities v= 0.1m/s, v = 0.26m/s, v= 0.28m/s, v= 0.3m/s, v =0.4 m/s and v= 0.5m/s, AOA starting from 2 to 14 degrees with the increment of 2 degrees and k-ℰ- Standard, k-ℰ -RNG and k-ℰ -Realizable models.
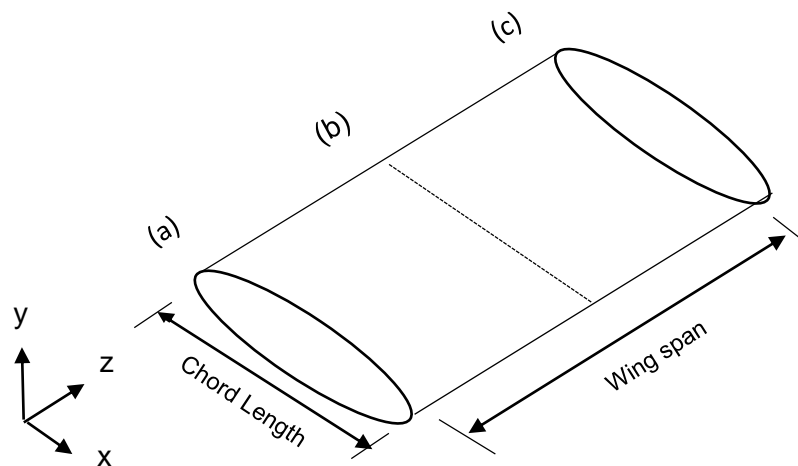

Figure 5-5 The 3D schematic view of the modified NACA0016 wing (a) is the point close to the fuselage of the underwater glider at Z= 1mm (b) is the point at the centre of the wing span at Z = 150mm and (c) is the point at the tip of the wing at Z= 300mm.

5.2.1   Surface distribution of the drag coefficient on the glider wing along the chord length

5.2.1.1 Influence of the AOA and the free stream velocities on the drag coefficient.
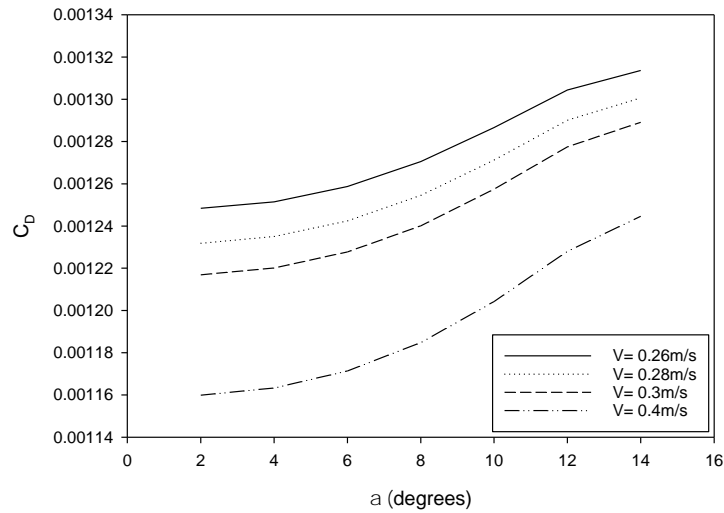
(a)
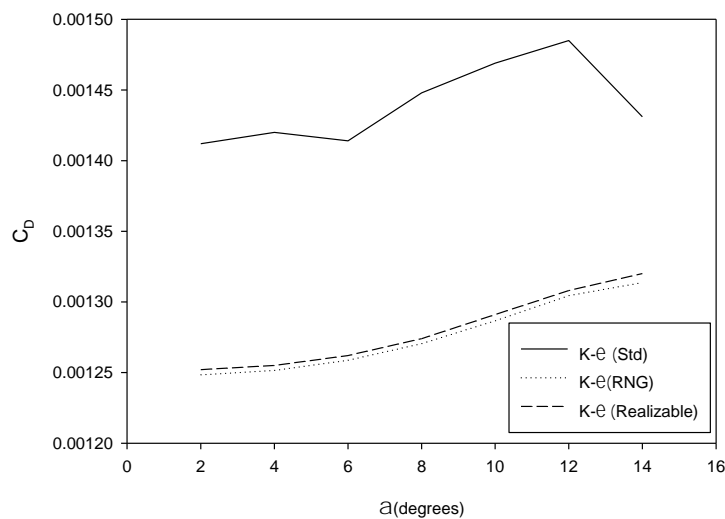
(b)

Figure 5-6 Drag coefficient as a function of the AOA (α) (a) at different inlet velocities for K-Ɛ (RNG) (b) turbulent models (c) AOAs

Figure 5.6 shows two sets of result namely: (a) C_D as a function of the AOA, and (b) the comparison of different turbulent models' predictions of the drag coefficient as a function of the AOA. It is observed that in figure (a) C_D increases as the AOA increases yielding a similar trend for different inlet velocities. This trend also suggest that C_D is the function of speed. The comparison of different inlet velocities showed the wing achieved more C_D at lower velocities than at the higher inlet velocities.(Abbott, n.d.)

In figure 5.6 (b) it is noticed that k-Ɛ (RNG) and k-Ɛ(Realizable) yielded almost similar results compared to k-Ɛ (Standard). The results also suggest for this type of study k-Ɛ (Standard) is not suitable.

5.2.2 Surface distribution of the lift coefficient on the glider wing

5.2.2.1 Influence of the aoa and the free stream velocities on the lift coefficient
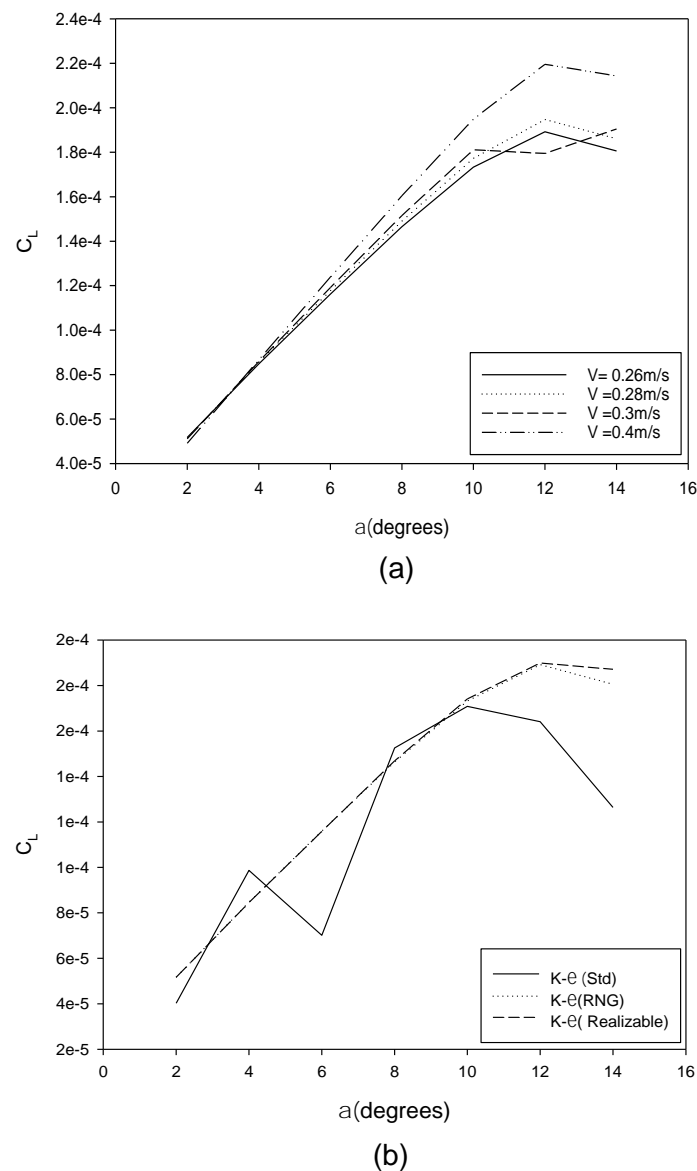

(a)

(b)

Figure 5-7 Lift coefficient as a function of the AOA (a) inlet velocities (b) turbulence models (c) AOAs

Figure 5.7 shows two set of results namely: (a) C_L as a function of the AOA, and (b) the comparison of different turbulent models' predictions of lift as a function of the AOA. The

results showed a similar trend for all inlet velocities, C_L increases as the AOA increases until reaches the maximum critical AOA after which it decreases. The critical AOA is defined as a stall or where the glider has no further lift beyond this point. It is observed that the glider wing reaches stalling point at approximately AOA =12 for all inlet velocities. Figure 5.7c also shows that the coefficient of lift shows that it is the function of velocity However, at 0.3m/s the trend shows some fluctuations which may be due to some level of solution instabilities occurring during the simulation. This can be caused by many factors such, relaxing factors, courant number etc.

Figure 5.7(b) shows the comparison of the three turbulent models and it is observed k-Ɛ (RNG) and K-Ɛ (Realizable) yielded the same results coming to the same stalling point whereas for k-Ɛ(Std) no distinct stalling point found. Therefore, it can be concluded for this type of work k-Ɛ(Std) is not suitable. Mackenzie did an investigation on the flow around submarine using three turbulent models, k-Ɛ (RNG), k-Ɛ (Realizable) and k-Ɛ(Standard), the results showed the k-Ɛ(Std) performed badly in this application and was considered not suitable for this type study which agrees with figure 5.7(b)

5.2.3 Surface distribution of the pressure coefficient on the glider wing along the chord length on three YX Planes (symmetry, mid-point and wing tip) along the span.

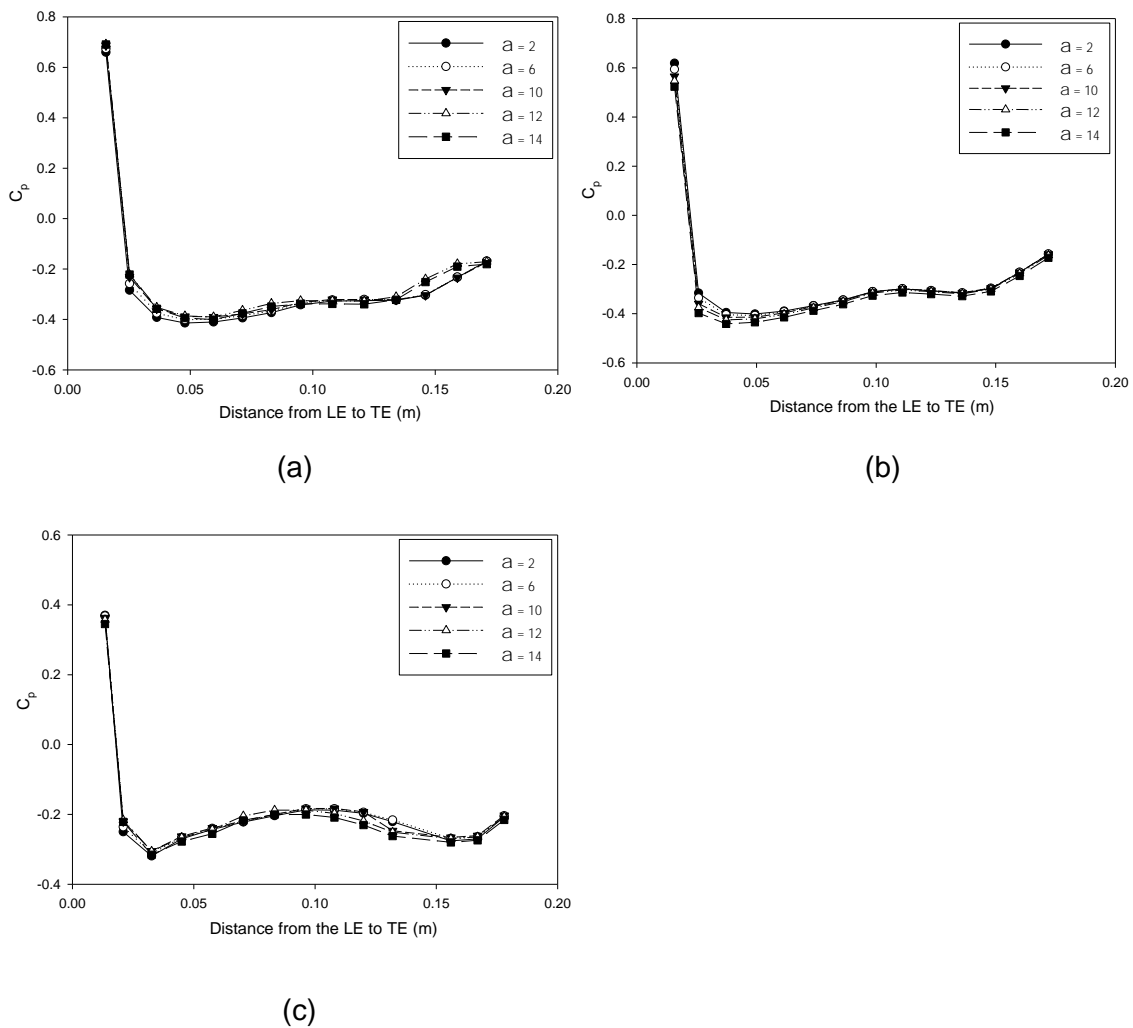### 5.2.3.1 Influence of the AOAs on the pressure coefficient.

(a)

(b)

(c)

Figure 5-8 Spatial Distribution of pressure coefficient as a function of the AOAs on three YX planes at Z=1mm, 150mm and 300 mm at a fixed inlet velocity of 0.3m/s for k-epsilon (RNG) model (a) fuselage (b) Mid-span (c) Tip-wing.

Figure 5.8 shows surface pressure distribution along the chord length in YX plane and along the wing span. The aerofoil wing is parameterized in three sections along the wing span as shown in figure 5.5. It is observed that the trend from figure 5.8(a) to figure 5.8(c) is consistent for all AOA with just minor differences. This trend is the consistent steep decrease of the pressure coefficient along the wing span and chord length. This behaviour is also in agreement with our CFD domain [see figure 5.1(a) to (d)] as there is higher pressure at the leading edge compared to the trailing edge. This kind of behaviour has been proven experimentally [(Haque et al., 2015) ;(Ladson et al., 1987)].

Table 5-1 Results summary of the influence of the AOA on C_p

	Fuselage	Mid-wing	Tip-wing	α (degrees)
C_{pMax}	0.69	0.65	0.38	2
C_{pMin}	-0.42	-0.41	-0.3	
C_{pMax}	0.7	0.6	0.38	6
C_{pMin}	-0.38	-0.41	-0.28	
C_{pMax}	0.72	0.58	0.37	10
C_{pMin}	-0.42	-0.41	-0.3	
C_{pMax}	0.72	0.55	0.37	12
C_{pMin}	-0.4	-41	-0.3	
C_{pMax}	0.72	0.53	0.36	14
C_{pMin}	-0.4	-0.48	-0.3	

It also noteworthy that at the tip of the wing, the values of C_p irrespective of the change in the AOA is relatively constant. The table also shows Cp at the fuselage is increasing with the AOA whereas at mid-wing it is decreasing.

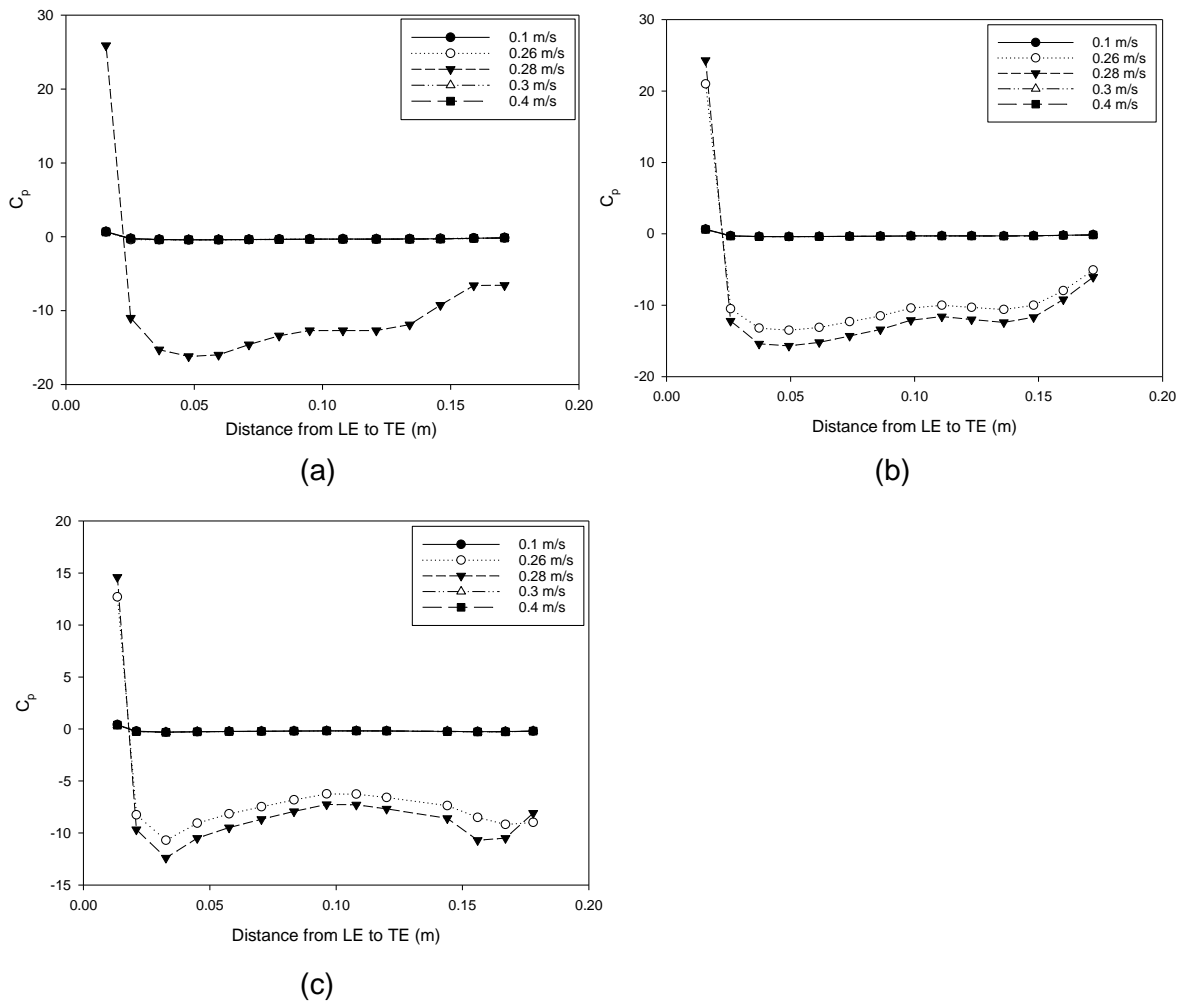## 5.2.3.2 Influence of the inlet velocities on the pressure coefficient

(a)

(b)

(c)

Figure 5-9 Spatial Distribution of pressure coefficient as a function of inlet velocities on three YX planes at Z=1mm, 150mm and 300 mm at a fixed AOA of 2 degrees for k-epsilon (RNG) model (a) fuselage (b) Mid span (c) Tip.

The surface distribution of pressure coefficient at different inlet velocities along the chord length in YX plane is presented in Figure 5.9. The wing is parameterized in the YX plane at three different sections along the wing span (a) Z=1mm, (b) Z=150mm and (c) Z=300mm. It is noticed that the spatial distribution of velocity along the chord length and along the span is not uniform. It is also observed from figure 5.9 (a) for inlet velocities of 0.1m/s, 0.26 m/s, 0.3 m/s and 0.4 m/s, the maximum C_p is the same at 0.2, whereas at 0.28m/s, it reaches a maximum C_p of 28.

Figure 5.9 (b) shows two distinct results whereby for the inlet speed of 0.1 m/s and 0.4 m/s the maximum C_p is approximately 0.2, whereas for 0.26 m/s and 028 m/s shows the maximum C_p of 23 and 26 respectively. Figure (c) also shows two similar distinct results, where for 0.1 m/s and 0.4 m/s the maximum C_p is 0.2 whilst 0.26m/s and 0.28m/s shows maximum C_p of 13

47

and 15 respectively. The overall summation can be said that the C_p is higher closer to the fuselage than at mid span and at the tip of the wing.

5.2.4 Hydrodynamic performance of the glider wing

5.2.4.1 Drag polar as a function of the AOA and the inlet velocities
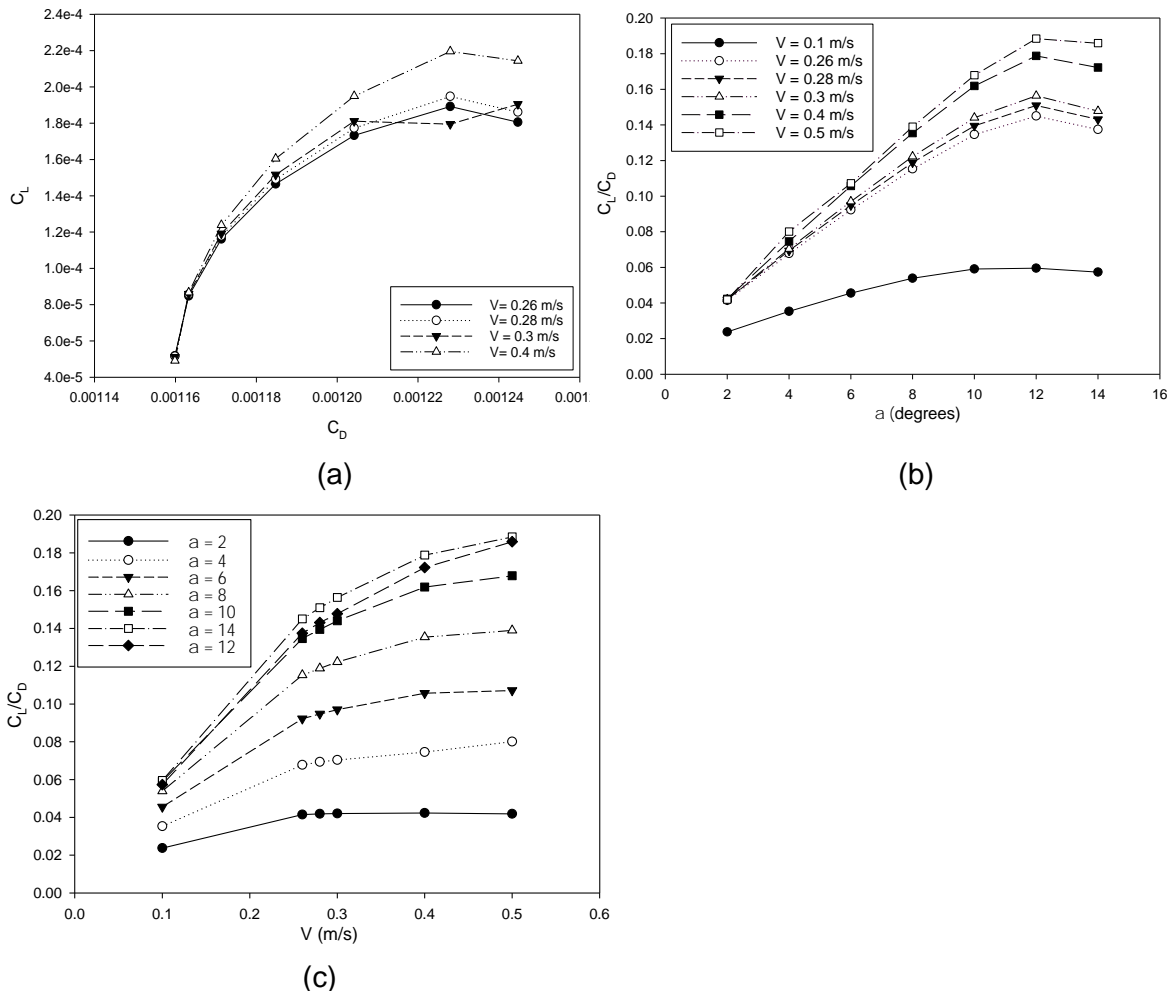

(a)

(b)

(c)

Figure 5-10 The graph shows YX plane (a) Drag polar for different inlet speeds (C_L vs C_D) (b) C_L/C_D vs AOA (c) C_L/C_D vs inlet velocities for k-Ɛ(RNG)

In optimizing the performance of the underwater glider wing, only the operating conditions such as inlet velocity and AOA are considered. The influence of the geometric properties of the aerofoil is not fully considered in this work as the aerofoil is of pre-defined form. Figure 5.10 (a) shows the drag polar performance at different AOA and different inlet velocities. The figures show that inlet velocities have a significant impact on the C_D and C_L. It can also be concluded that the minimal drag polar is around the inlet velocity of 0.26 m/s, which can be selected as the optimal design point.

Figure 5.10 (b) shows C_L/C_D ratio as the function of the AOA varies with inlet speeds. It is noticed that for both figure 5.10 (b) and figure 5.7(a), the critical AOA of attack is approximately 12. Figure 5.10 (c) shows how C_L/C_D ratio as the function of speed varies with the different AOAs. It can be seen form the chart that gradually increases with the inlet velocities with the largest increase recorded at higher angles of attack.

5.2.5   Influence of the farfield boundary on the numerical results

It is well established that the farfield boundary conditions can affect the numerical predictions of an aerofoil subjected to hydrodynamic force. However, the domain size in this study has been carefully chosen to minimise this effect. Therefore, the effects of the farfield boundary conditions on the numerical results has not been considered in this study.

CHAPTER 6

CONCLUSION

Underwater glider wings are the lifting surfaces with the chosen aerofoil sections. The efficiency as well as the performance of an underwater glider mostly depends on the hydrodynamic characteristics e.g. lift, drag, lift to drag ratio, etc on the wings. Besides many factors, the effects of wing shape are also crucial to the design and underwater glider performance. This study presents the numerical investigation to explore the hydrodynamic performance improvement obtained by incorporating curvature at the trailing edge of a wing as oppose to the standard straight or sharp trailing edge.

A CAD model with straight leading edge and trailing edge i.e. rectangular planform was prepared with NACA 0016 using SolidWorks 2017. The operating conditions were setup such that the inlet velocities varies from 0.1 m/s ,0.26 m/s ,0.28 m/s ,0.3 m/s ,0.4m/s and 0.5 m/s corresponding to a Reynolds number of 27.8 x 103 and 53 x 103.The static pressure at different angles of attack (AOA) ranging from 2 to 16 degrees at the increment of 2degrees for three turbulent models i.e. k-Ɛ (standard), k-Ɛ (RNG) and k-Ɛ (Realizable) was calculated for both upper and lower surfaces of the modified wing model using ANSYS Fluent 18.1.

Thereafter the static pressure distribution, lift coefficient, drag coefficient, lift to drag ratio and pressure coefficient for both upper and lower surfaces were analysed and the following can be concluded from this study:

- The lift and drag coefficient are a function of the AOA and free stream velocities. If these parameters change the performance of the underwater glider and its hydrodynamic behaviour changes.
- The underwater glider wing is optimized using the C_L/C_D ratio as function of the AOA and inlet velocities. The investigation showed the optimal design point of the AOA of 12 degrees at the corresponding speed of 0.26m/s. This is also shown in figure 5.8 (a) which shows the C_L as the function of the AOA. The critical AOA matched with the optimal design point of 12degrees.
- It is also observed that Cp varies across the wing span. The results showed the Cp is higher closer to the fuselage and decreases in the mid and at the tip of the wing. This can mean the wing experience more stress close to the fuselage than the rest of the wing span. This therefore explains why more structural rigidity must be provided in this region of high stress (pressure force) concentration.
- In the case of two equation models, the turbulence model with more accurate predictions are the K-Ɛ(RNG) and K-Ɛ (Realizable) models.

- The drag and lift curve corresponded to the typical wing characteristics of the published experiment data irrespective of the fluid medium and operating conditions.

CHAPTER 7

BIBLIOGRAPHY

Abbott, B.I.R.A.H. THEORY OF Including a Summary of Airfoil Data.

Ahmed, S. 2013. 0012 Wing Flapped at Different Flap Angles with. , 13(4).

Anon. No Title.

Anon. Lifting-line theory class notes.

Anon. 1 . Fluid Dynamics Around Airfoils 2 . Governing Equations. : 1–10.

Anon. Module G: Turbulent Compressible / Incompressible Flow Over an Isolated Airfoil.

Arvin, I., Branch, K., Numbers, R., Arvin, I. & Toghraie, D. 2016. 3D Simulation of turbulent Flow over Three Different Airfoils in Different Reynolds Numbers 2 nd International Congress of Recent Advances in Engineering ICRAE2014 3D Simulation of turbulent Flow over Three Different Airfoils in Different. , (February 2014): 1–7.

Aeronautics, N. 1977. Aerodynamic of Wing-Body With Characteristics Configuration Advanced General Sections and simple flap systems.

Azim, R., Hasan, M.M. & Ali, M. 2015. Numerical investigation on the delay of boundary layer separation by suction for NACA 4412. *Procedia Engineering*, 105(Icte 2014): 329–334. http://dx.doi.org/10.1016/j.proeng.2015.05.013.

Barakos, G.N. & Drikakis, D. 2000. Unsteady separated flows over manoeuvring lifting surfaces. The Royal Society, 358: 3279–3291.

Battaglia, F. & Paul, M.R. 2014. 3D Dynamic Stall Simulation of Flow Over Naca0012 Airfoil At 10 5 and 10 6 Reynolds Numbers.

Bender, A., Steinberg, D.M., Friedman, A.L. & Williams, S.B. 2008. Analysis of an Autonomous Underwater Glider. *Australasian Conference on Robotics and Automation 2008 (ACRA 08)*: 1–10. ftp://soest.hawaii.edu/bhowe/outgoing/For_Brian_S/Presentations/NavPapers-SWebster/bender-2008-usyd-glidermodel.pdf.

Bertram, V. 2012. Practical Ship Hydrodynamics. *Practical Ship Hydrodynamics*.

Bhatta, P. & Leonard, N.E. 2002. Stabilization and coordination of underwater gliders. Proceedings of the 41st IEEE Conference on Decision and Control, 2002., 2: 2081–2086. http://ieeexplore.ieee.org/lpdocs/epic03/wrapper.htm?arnumber=1184836.

Bhargava, V., Dwivedi, Y. & Rao, P. 2017. Analysis of Multi-Element Airfoil Configurations: A Numerical Approach. MOJ Applied Bionics and Biomechanics, 1(2): 7. http://medcraveonline.com.

Canonsburg, A.D. 2017. ANSYS Fluent User ' s Guide. , (January).

Cimbala and Cengel. 2009. *Fluid Dynamics*.

Davis, R., Eriksen, C. & Jones, C. 2002. Autonomous buoyancy-driven underwater gliders. *… Applications of Autonomous Underwater …*: 1–11. http://www.ifremer.fr/lpo/gliders/donnees_tt/references/techno/4Gliders.pdf.

Diego, U.C.S., Scott, A. & Douglas, E. Scripps Institution of Oceanography.

Diab, H., Younes, R. & Lafon, P. 2017. Survey of research on the optimal design of sea harbours. International Journal of Naval Architecture and Ocean Engineering, 9(4): 460–472. http://dx.doi.org/10.1016/j.ijnaoe.2016.12.004.

Division, S. & Undersea, N. 2002. Maneuvering Hydrodynamics of Fish and Small Underwater Vehicles 1. , 117: 102–117.

Dod, D.C.P. 1946. LIMITATION CHANGES TO : FROM : NASA TR Server website.

Dwivedi, Y.D., Prasad, M.S. & Dwivedi, S. 2018. Experimental Aerodynamic Static Stability Analysis of Different Wing Planforms. , (April).

Executive, P. & Defence, M.O.F. PROCUREMENT EXECUTIVE , MINISTRY OF DEFENCE The Nature , Development and Effect of the Viscous an Aerofoil with Flow around High - Lift Devices. , (1258).

Fan, S. & Woolsey, C.A. 2014. Dynamics of underwater gliders in currents. Ocean Engineering, 84: 249–258. http://dx.doi.org/10.1016/j.oceaneng.2014.03.024.

Fulvio Bellobuono Tutor Coordinator Domenico Coiro Antonio Moccia, E.P. 2006. Aircraft Endurance Improvement Through Turbulent Separation Control. , (December).

Gómez, A. & Pinilla, Á. 2006. Aerodynamic Characteristics of Airfoils with Blunt Trailing Edge. *Revista de Ingeniería*, (24): 23–33. http://www.scielo.org.co/scielo.php?script=sci_arttext&pid=S0121-49932006000200004&lng=en&nrm=iso&tlng=en.

Gliders, A.U. 2008. Autonomous Underwater Gliders.

Haque, M.N., Ali, M. & Ara, I. 2015. Experimental investigation on the performance of NACA 4412 aerofoil with curved leading edge planform. *Procedia Engineering*, 105(Icte 2014): 232–240. http://dx.doi.org/10.1016/j.proeng.2015.05.099.

Hussain, N.A.A., Arshad, M.R. & Mohd-Mokhtar, R. 2011. Underwater glider modelling and analysis for net buoyancy, depth and pitch angle control. *Ocean Engineering*, 38(16): 1782–1791. http://dx.doi.org/10.1016/j.oceaneng.2011.09.001.

Ichihashi, N., Ikebuchi, T. & Arima, M. 2008. Development of an Underwater Glider with Independently Controllable Main Wings. Proceedings of the International Offshore and Polar Engineering Conference, 8: 156–161.

Isa, K. & Arshad, M.R. 2012. Buoyancy-driven underwater glider modelling and analysis of motion control. Indian Journal of Marine Sciences, 41(6): 516–526.

Jagadeesh, P., Murali, K. & Idichandy, V.G. 2009. Experimental investigation of hydrodynamic force coefficients over AUV hull form. *Ocean Engineering*, 36(1): 113–118.

Javaid, M.Y., Ovinis, M., Hashim, F.B.M., Maimun, A., Ahmed, Y.M. & Ullah, B. 2017. Effect of wing form on the hydrodynamic characteristics and dynamic stability of an underwater glider. *International Journal of Naval Architecture and Ocean Engineering*, 9(4): 382–389. http://dx.doi.org/10.1016/j.ijnaoe.2016.09.010.

Javaid, M.Y., Ovinis, M., Hashim, F.B.M., Maimun, A., Ahmed, Y.M. & Ullah, B. 2016. Effect of wing form on the hydrodynamic characteristics and dynamic stability of an underwater glider. *International Journal of Naval Architecture and Ocean Engineering*. http://linkinghub.elsevier.com/retrieve/pii/S2092678216304691.

Jeong, D.H., Roh, M. II, Ham, S.H. & Lee, C.Y. 2017. Performance analyses of naval ships based on engineering level of simulation at the initial design stage. International Journal of Naval Architecture and Ocean Engineering, 9(4): 446–459.

http://dx.doi.org/10.1016/j.ijnaoe.2016.12.002.

Jones, D.A. & Clarke, D.B. 2005. Simulation of a Wing-Body Junction Experiment using the Fluent Code. Platforms Sciences Laboratory.

Jones, D.A. 1970. The Calculation of Hydrodynamic Coefficients for Underwater Vehicles. Program, 76(16): 3–6.

Kato, N. Mini Underwater Glider (MUG) for Education.

Kesel, a B. 2000. Aerodynamic characteristics of dragonfly wing sections compared with technical aerofoil. The Journal of experimental biology, 203(Pt 20): 3125–35. http://www.ncbi.nlm.nih.gov/pubmed/11003823.

Khan, M.I. & Al-faruk, A. 2018. Comparative Analysis of Aerodynamic Characteristics of Rectangular and Curved Leading Edge Wing Planforms American Journal of Engineering Research (AJER). , (5).

Kopaç, M., Yılmaz, M. & Gültop, T. 2005. An Investigation of the Effect of Aspect Ratio on the Airfoil Performance. American Journal of Applied Sciences, 2(2): 545–549. http://scholar.google.com/scholar?hl=en&btnG=Search&q=intitle:An+Investigation+of+the+Effect+of+Aspect+Ratio+on+the+Airfoil+Performance#0.

Kroo, I. 2005. NONPLANAR WING CONCEPTS FOR INCREASED AIRCRAFT EFFICIENCY Introduction, Assessing the Potential.: 1–29.

Lloyd, G. & Espanoles, a. 2002. Best practice guidelines for marine applications of computational fluid dynamics. Consultants and Members of the NSC, MARNET-CFD http://scholar.google.com/scholar?hl=en&btnG=Search&q=intitle:best+practice+guidelines+for+marine+applications+of+computational+fluid+dynamics#0%5Cnhttp://scholar.google.com/scholar?hl=en&btnG=Search&q=intitle:Best+practice+guidelines+for+marine+applicati.

Mary, Q. 2000. Unsteady separated flows over manoeuvring lifting surfaces.

Menter, F.R., Kuntz, M. & Langtry, R. 2003. Ten Years of Industrial Experience with the SST Turbulence Model. Turbulence Heat and Mass Transfer 4, 4: 625–632. http://cfd.mace.manchester.ac.uk/flomania/pds_papers/file_pds-1068134610Menter-SST-paper.pdf.

Meyer, D. 2016. Glider Technology for Ocean Observations: A Review. Ocean Science Discussions, (July): 1–26. http://www.ocean-sci-discuss.net/os-2016-40/.

Milgram, J.H. Strip Theory for Underwater Vehicles in Water of Finite Depth.

Munk, M.M. 1923. General Theory of Thin Wing Sections. *National Advisory Committee for Aeronautics*, (142): 243–261.

Nichols, R.H. Turbulence Models and Their Application to Complex Flows University of Alabama at.

One, T. 1952. UNCLASSIFIED.

Panaras, A.G. 2015. Numerical Simulation of Airfoil Flow at High Angle of Attack. *Journal of Vortex Science and Technology*, 02(02). https://www.omicsonline.com/open-access/numerical-simulation-of-airfoil-flow-at-high-angle-of-attack-2090-8369-1000116.php?aid=60304.

Pneumatically, T.O.F.A., Underwater, P. & For, G. 2015. *Design and Testing of a Pneumatically Propelled Underwater Glider for Shallow Water*.

Rahimi, H., Medjroubi, W., Stoevesandt, B. & Peinke, J. 2014. 2D Numerical Investigation of the Laminar and Turbulent Flow Over Different Airfoils Using OpenFOAM. *Journal of Physics: Conference Series*, 555(1): 012070. http://stacks.iop.org/1742-6596/555/i=1/a=012070.

Raj, S. & Chandra, S. 2014. Advancement in autonomous underwater vehicles: Design &; performance perspective. *19th Offshore Symposium 2014: Emerging Technologies in Offshore Drilling and Production*, (February): 374–380. https://www.scopus.com/inward/record.uri?eid=2-s2.0-84942163573&partnerID=40&md5=a7581caae16195fe2cad6f6db506302d.

Rudnick, D.L., Davis, R.E., Eriksen, C.C. & Fratantoni, D.M. Full-Text. : 48–59.

Riegels, F.W. 1961. Aerofoil Sections results from wind-tunnel investigations theoretical foundations.

Selig, M.S. 2003. Low Reynolds Number Airfoil Design Lecture Notes - Various Approaches to Airfoil Design. Low Reynolds Number Airfoil Design Lecture Notes - Various Approaches to Airfoil Design, (November): 24–28. http://www.ae.illinois.edu/m-selig/pubs/Selig-2003-VKI-LRN-Airfoil-Design-Lecture-Series.pdf.

Sherman, J., Davis, R.E., Owens, W.B. & Valdes, J. 2001. The autonomous underwater glider. Oceanic Engineering, IEEE Journal of, 26(4): 437–446.

Shi, Y., Pan, G., Jiang, J., Shi, Y. & Pan, G. 2013. Computation of Hydrodynamic Coefficients of Portable Autonomous Underwater Vehicle. : 2013.

Singh, Y., Bhattacharyya, S.K. & Idichandy, V.G. 2017. CFD approach to modelling, hydrodynamic analysis and motion characteristics of a laboratory underwater glider with experimental results. *Journal of Ocean Engineering and Science*, 2(2): 90–119. http://linkinghub.elsevier.com/retrieve/pii/S2468013316300729.

Stockdill, B., Pedro, G., Suleiman, A., Magagnato, F. & Djilali, N. 2006. Simulation of Unsteady Turbulent Flow Over a Stalled Airfoil. Computational Fluid Dynamics Journal, 14(4): 359–378.

Sun, C., Song, B. & Wang, P. 2015. Parametric geometric model and shape optimization of an underwater glider with blended-wing-body. International Journal of Naval Architecture and Ocean Engineering, 7(6): 995–1006. http://dx.doi.org/10.1515/ijnaoe-2015-0069.

Theodorsen, T. 1932. Theory of wing sections of arbitrary shape. NACA Report. http://www.pdas.com/refs/rep411.pdf.

Thomareisa, N. & Papadakis, G. 2017. Effect of trailing edge shape on the separated flow characteristics around an airfoil at low reynolds number: A numerical study. *Physics of Fluids*, 29(1).

Versteeg and Malasekera. 2007. *Computational Fluid Dynamics*.

van de Wal, H.J.B. 2010. Design of a Wing with Boundary Layer Suction. : 155.

Vols, F., Our, A. & Engineering, O. Numerical Simulations Techniques applied to Coastal and Oceanographic Engineering - Computational Fluid Dynamics (CFD). Direct: 1–6.

Wang, C. & Anvar, A. 2012. Modeling and Simulation of Motion of an Underwater Robot Glider for Shallow-water Ocean Applications. : 18–21.

Wang, H., Teo, C.J., Khoo, B.C. & Goh, C.J. 2013. Computational aerodynamics and flight stability of Wing-In-Ground (WIG) craft. Procedia Engineering, 67: 15–24. http://dx.doi.org/10.1016/j.proeng.2013.12.002.

Wiebe, J.P., Beausoleil, M., Zhang, G. & Cialacu, V. 2010. Journal of Steroid Biochemistry and Molecular Biology Opposing actions of the progesterone metabolites 118(1): 125–132.

Xie, Y., Yang, C., Wang, P., Peng, S., Fan, S. & Zhang, S. 2013. Improved Performance of an Underwater Glider with Passively Rotatable Wings. , (3): 0–4.

Y, T.O.N.C.C.X. & Hickman, A. 1943. National Advisory Committee for Aeronautics. Journal of Applied Physics, 14(8): 399. http://link.aip.org/link/JAPIAU/v14/i8/p399/s1&Agg=doi.

You, D. & Bromby, W. 2012. Large-Eddy Simulation of Unsteady Separation Over a Pitching Airfoil at High Reynolds Number. Seventh International Conference on Computational Fluid Dynamics (ICCFD7): 1–9.

Zalovcik, B.J.A., Wood, C., Memorial, L. & Field, L. Wartime report.

Zhang, S., Yu, J., Zhang, A. & Zhang, F. 2013. Spiraling motion of underwater gliders: Modeling, analysis, and experimental results. *Ocean Engineering*, 60: 1–13. http://dx.doi.org/10.1016/j.oceaneng.2012.12.023.

Zhang, F., Zhang, F. & Tan, X. 2012. Steady Spiraling Motion of Gliding Robotic Fish. : 1754–1759.

Zimmerman,C.H. 1932. Characteristics of Clark Y Airfoils of Small Aspect Ratios. National Advisory Committee for Aeronautics, Langley Memorial Aeronautical Laboratory: 581. http://naca.central.cranfield.ac.uk/reports/1933/naca-report-431.pdf.

APPENDICES

APPENDIX A
STANDARD K-Ɛ TURBULENT PARAMETERS RESULTS

TURBULENT KINETIC ENERGY RESULTS

Figure A 1 shows YX Plane Turbulent kinetic energy for standard K-Ɛ model for the velocity of 0.26 m/s at AOA = 2.
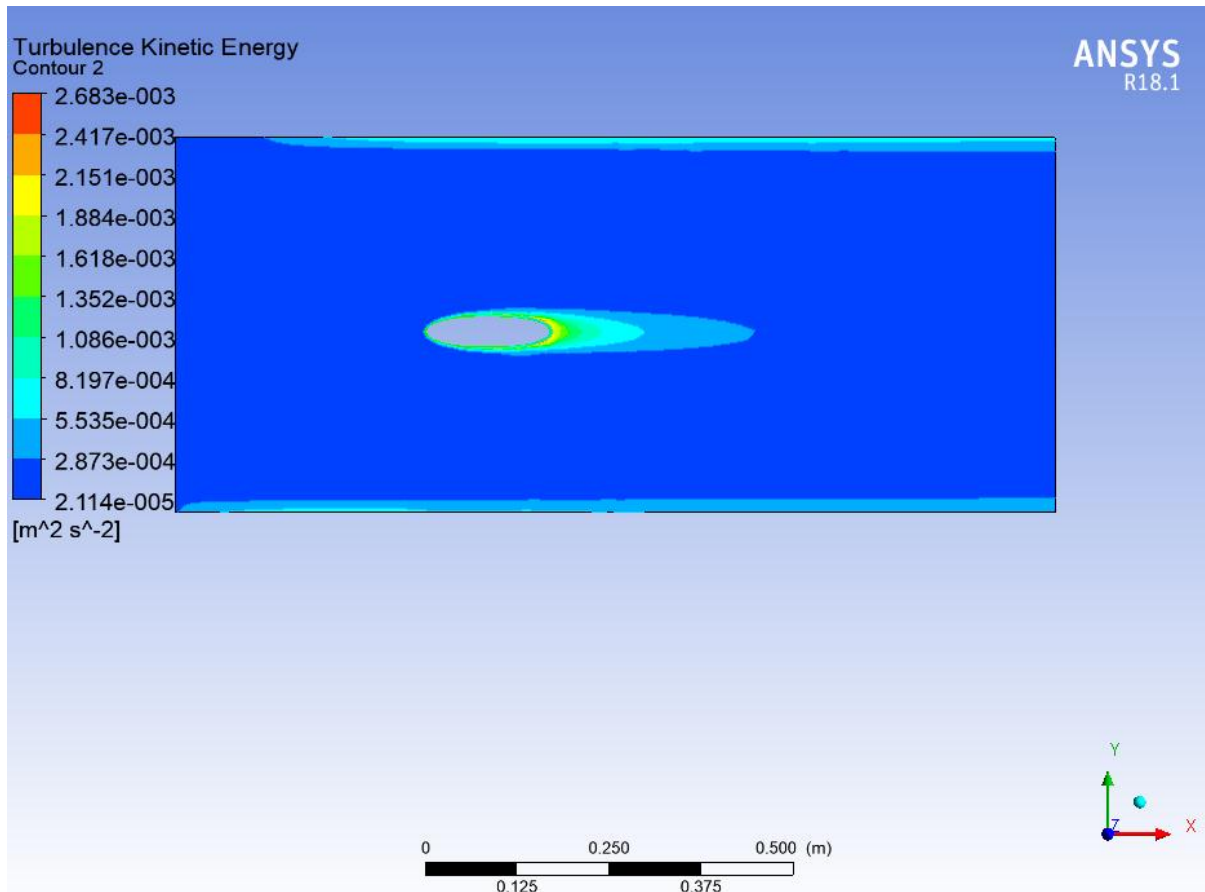
Figure A-1 Turbulent Kinetic Energy at X= 1mm (Close to the Fuselage)

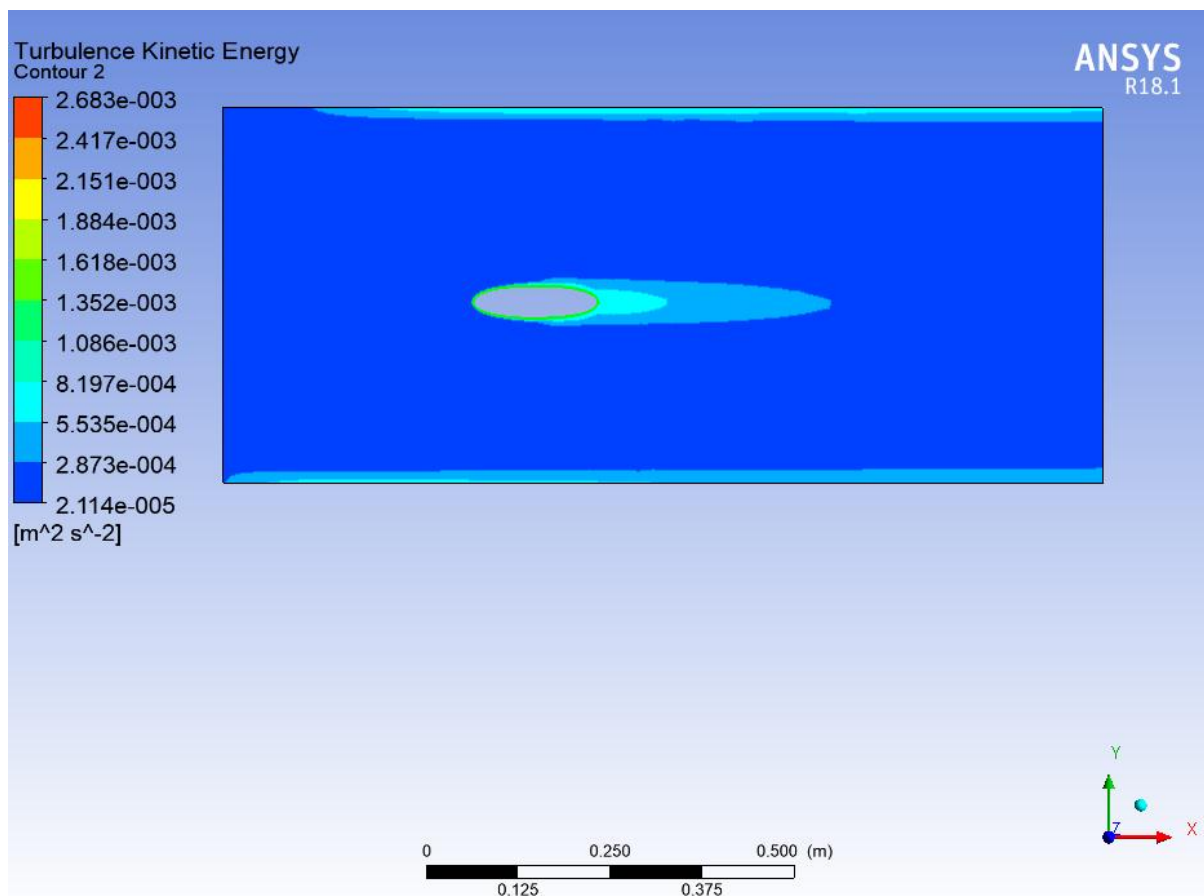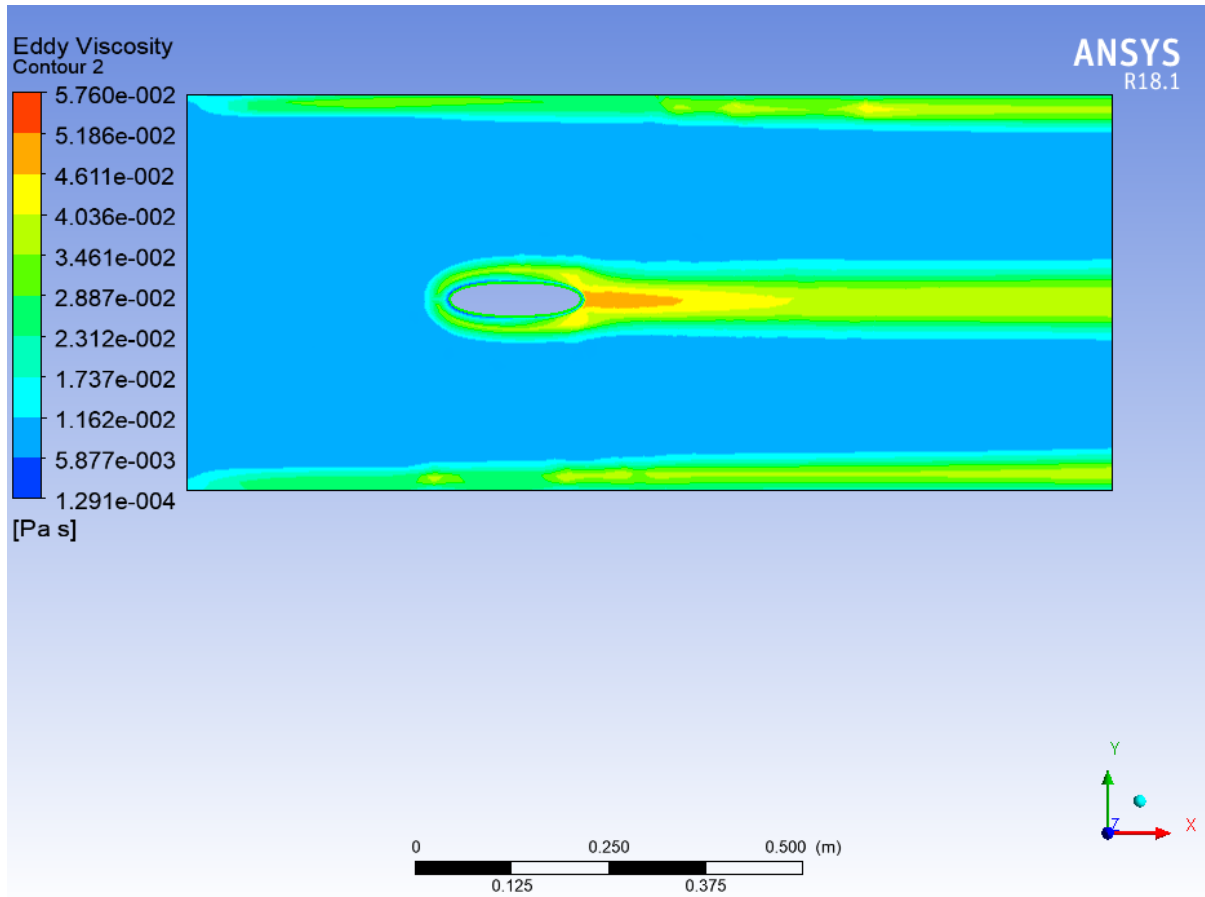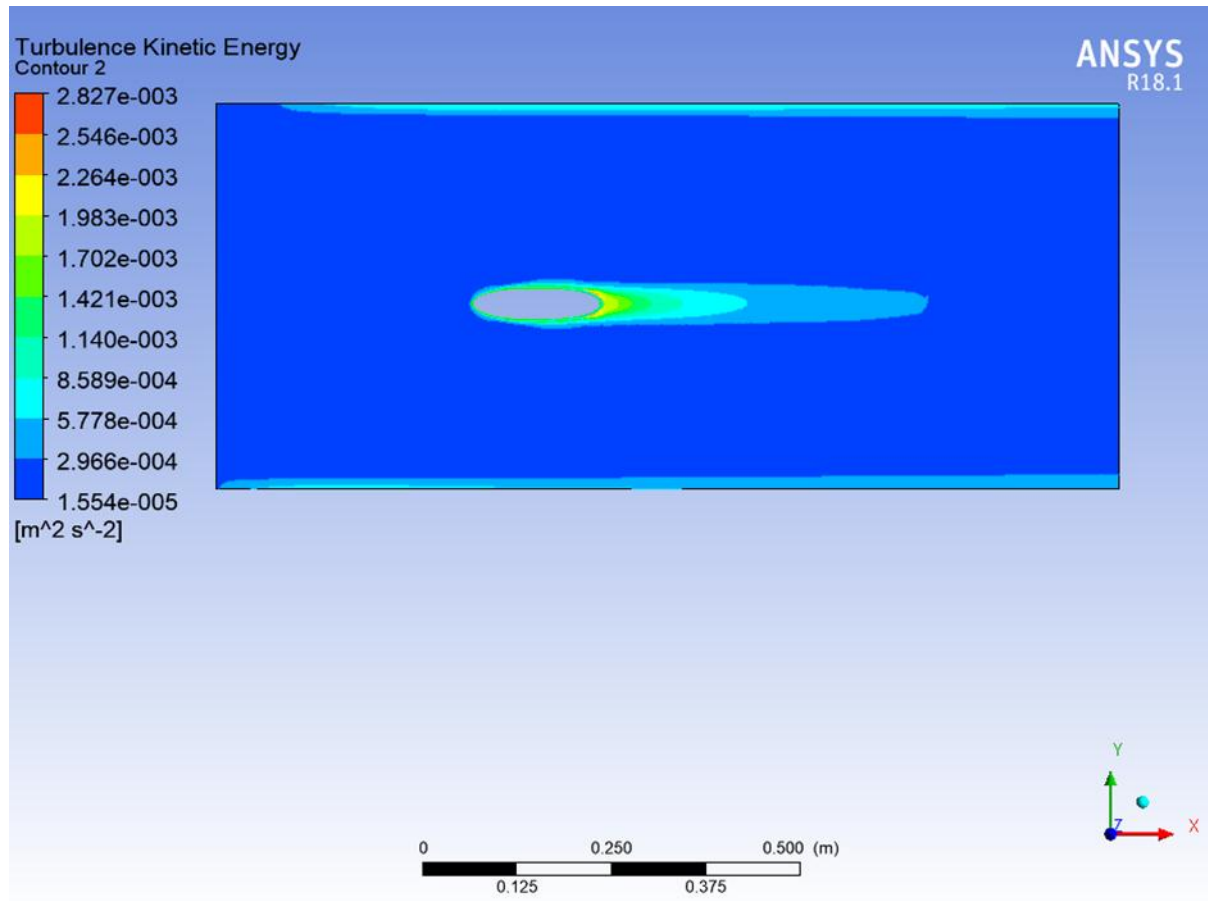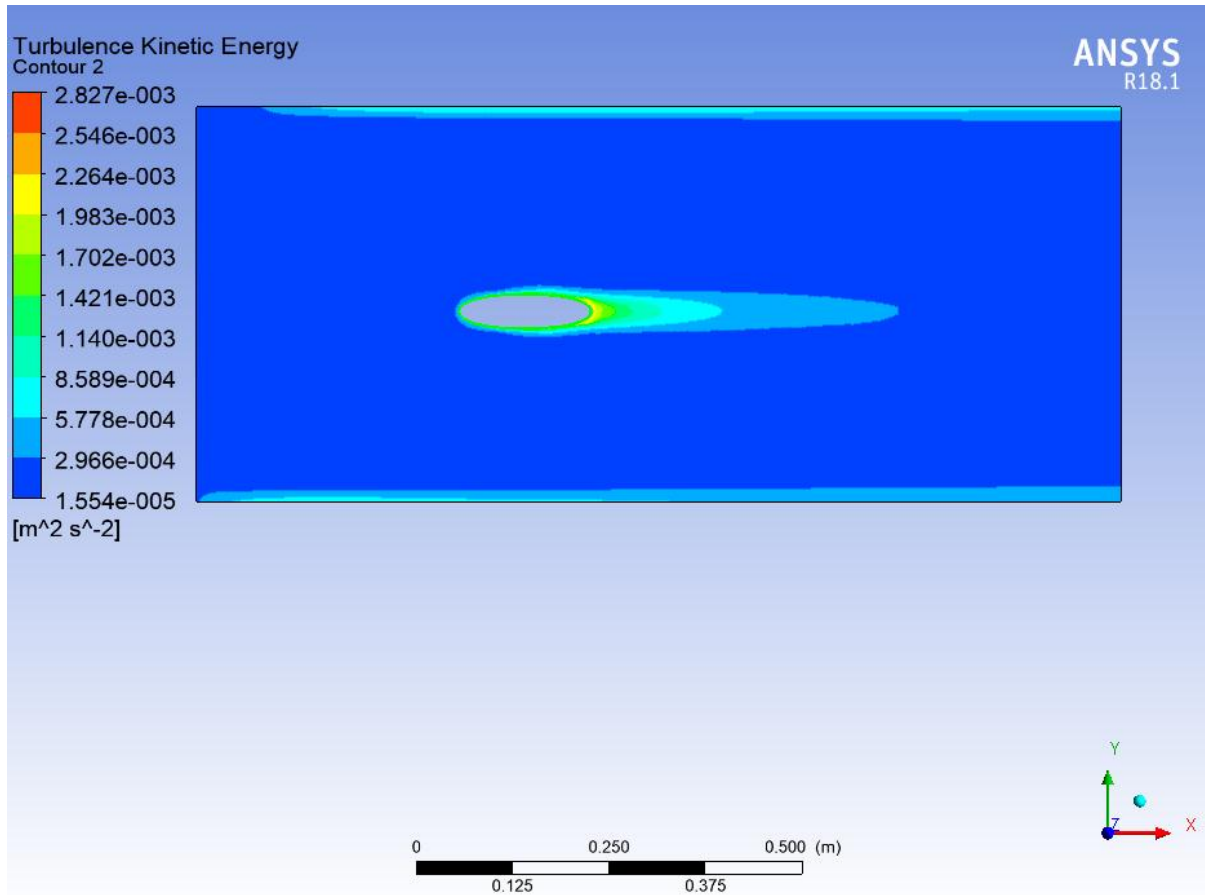Figure A 2 shows YX Plane Turbulent kinetic energy for standard K-Ɛ model for the velocity of 0.26 m/s at AOA = 2.
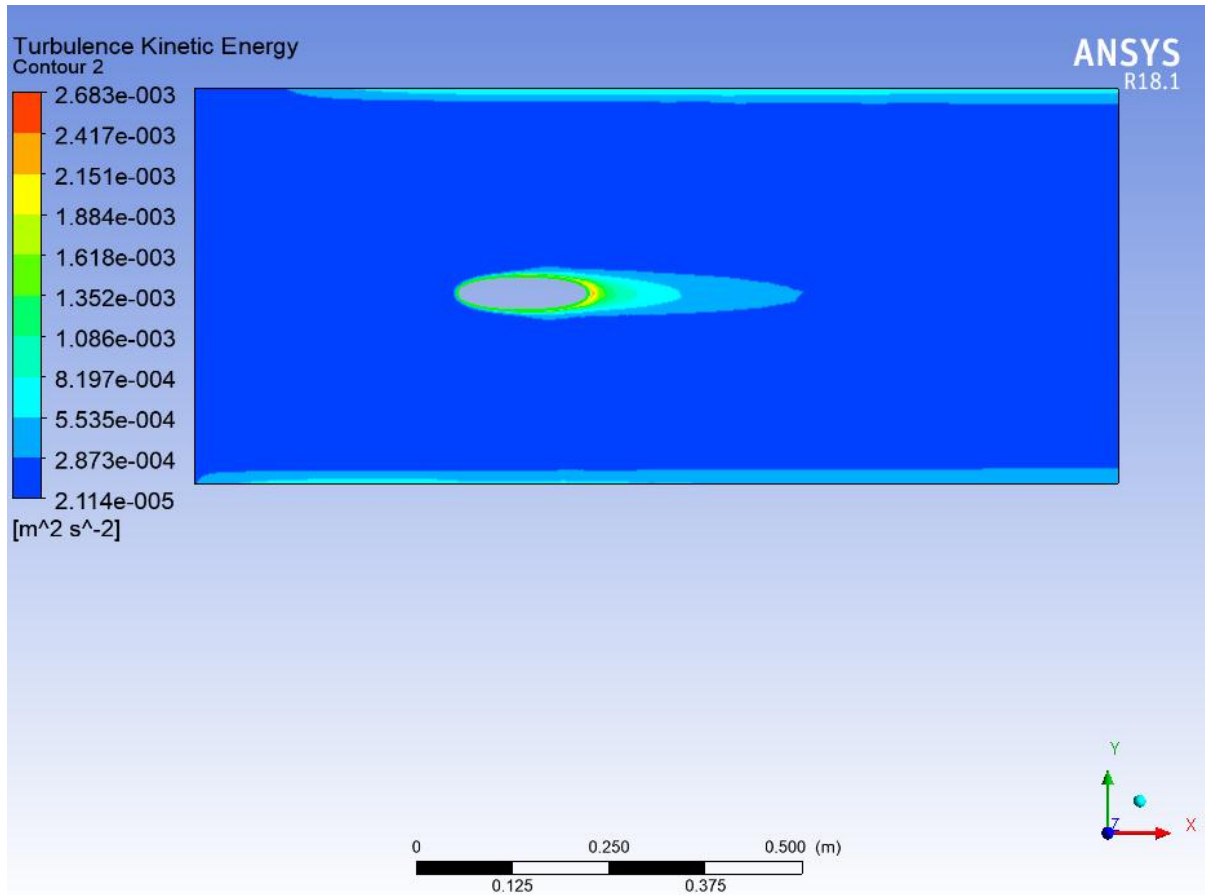
Figure A-2 Turbulent Kinetic Energy at X= 150 mm (Mid-Wing)

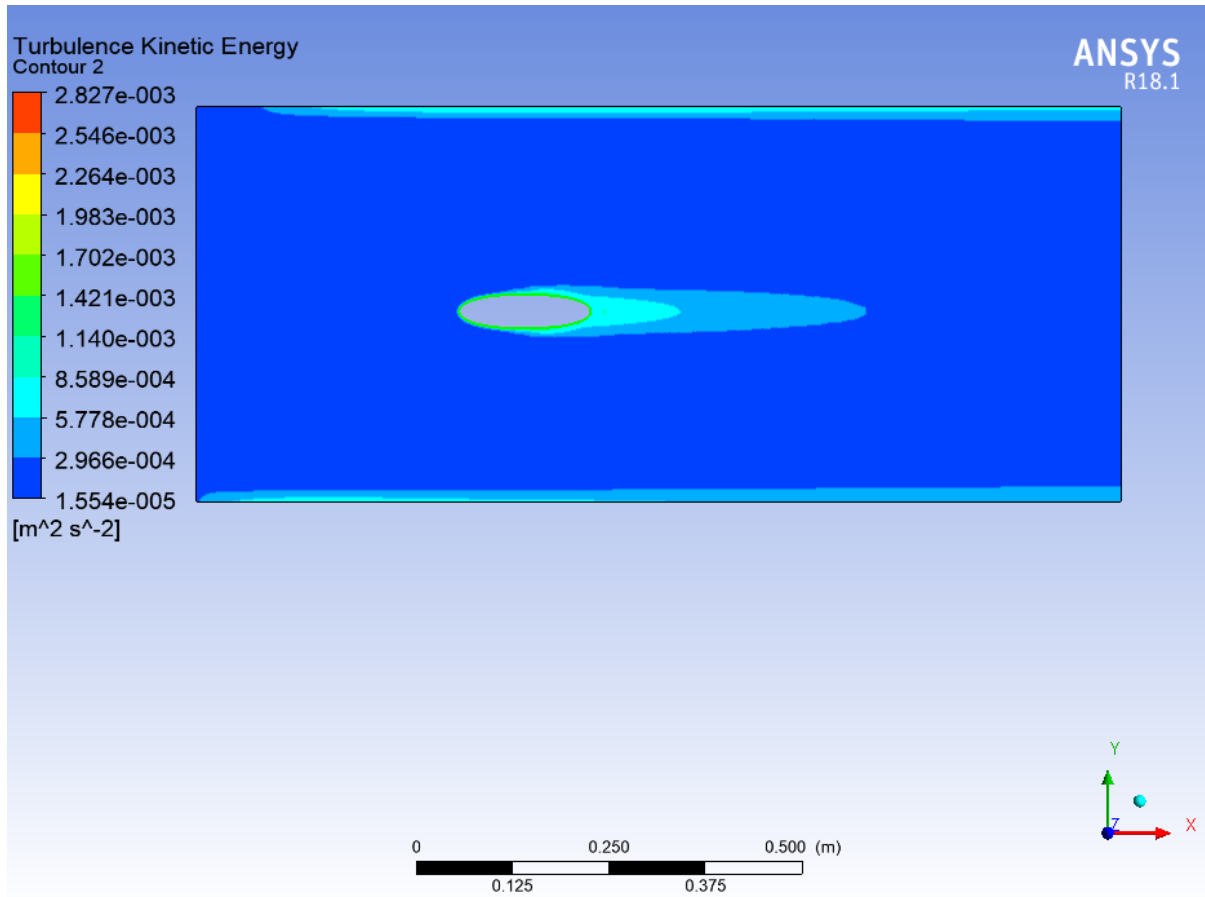Figure A 3 shows YX Plane Turbulent kinetic energy for standard K-Ɛ model for the velocity of 0.26 m/s at AOA = 2.

Figure A-3 Turbulent Kinetic Energy at X= 300 mm (Tip-Wing)

EDDY VISCOSITY RESULTS – K-Ɛ(Standard)

Figure A 4 shows YX Plane Eddy Viscosity for standard K-Ɛ model for the velocity of 0.26 m/s at AOA = 2.
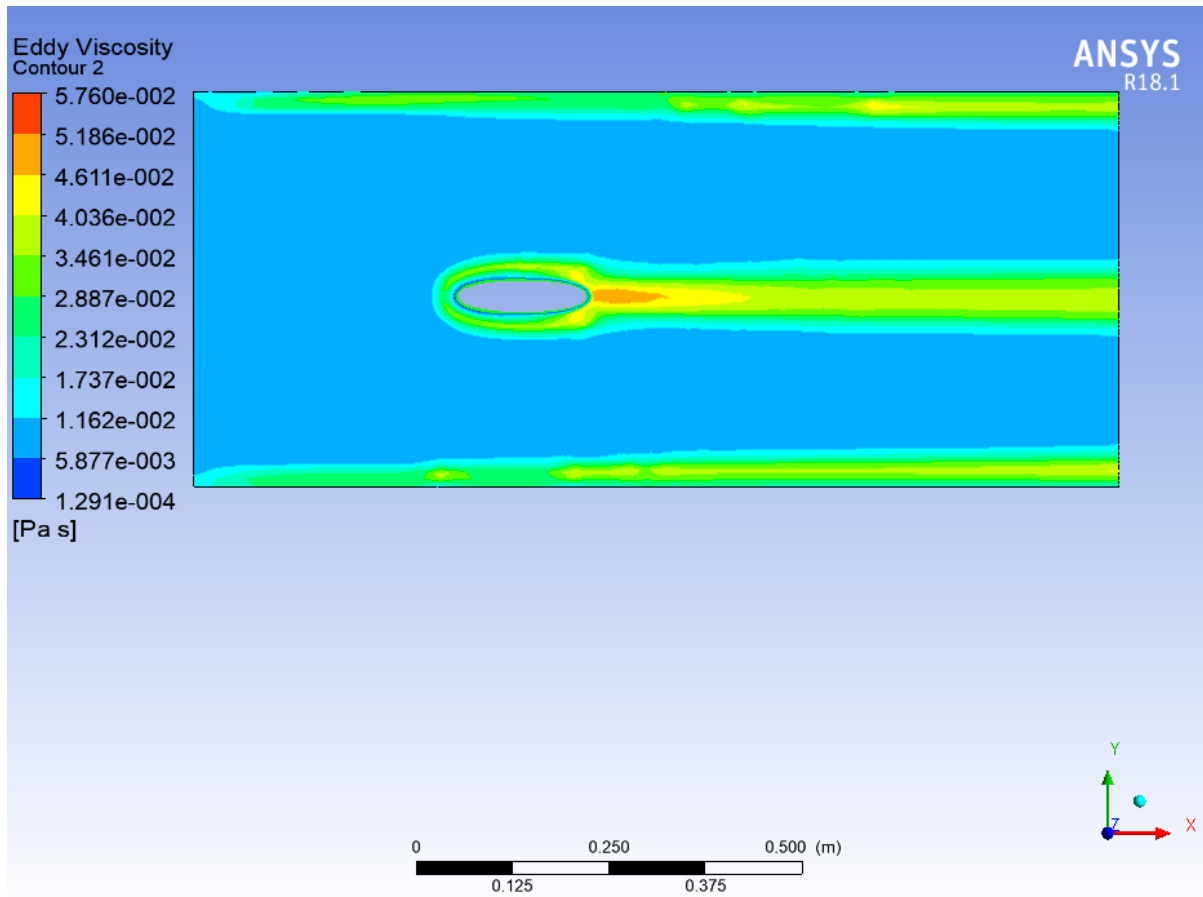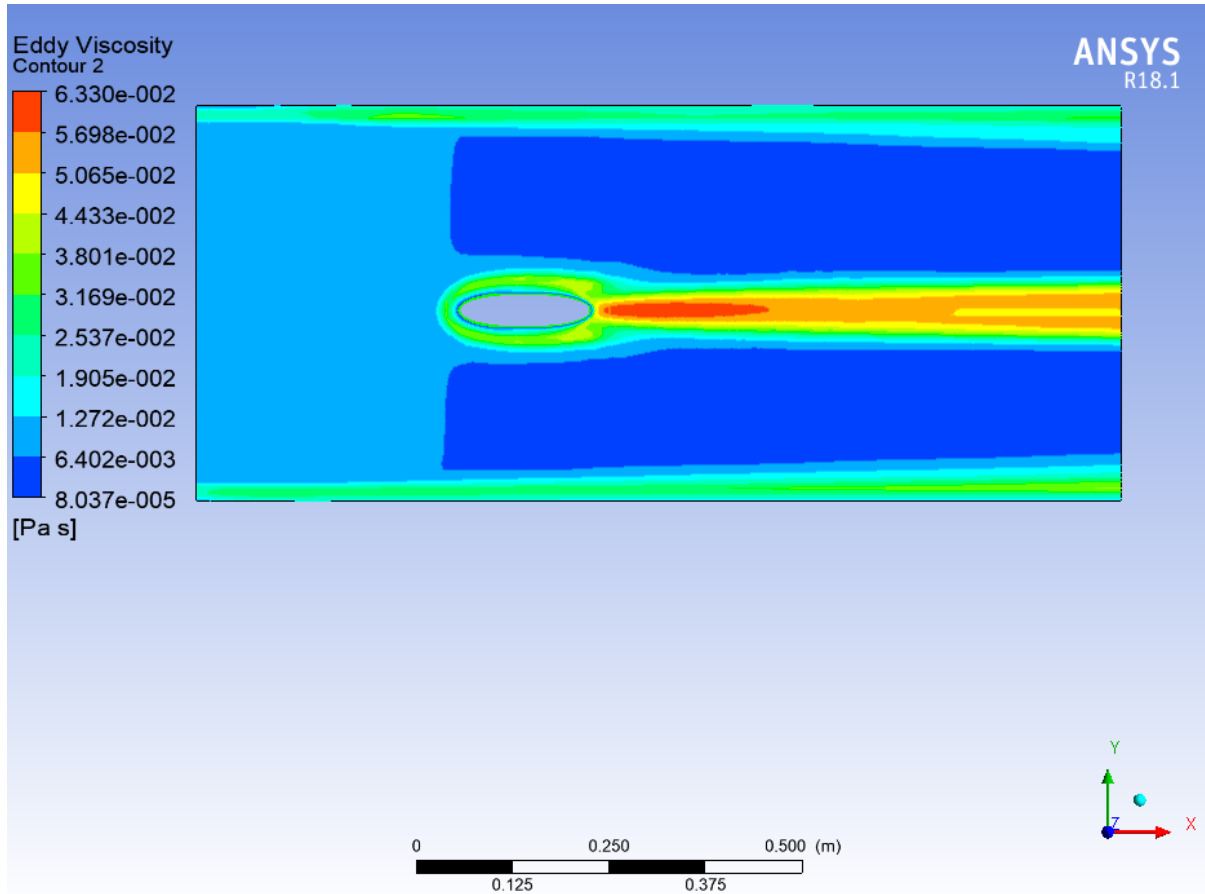

Figure A-4 Eddy Viscosity at X= 1mm (close to the fuselage)

Figure A 5 shows YX Plane Eddy Viscosity for standard K-Ɛ model for the velocity of 0.26 m/s at AOA = 2.
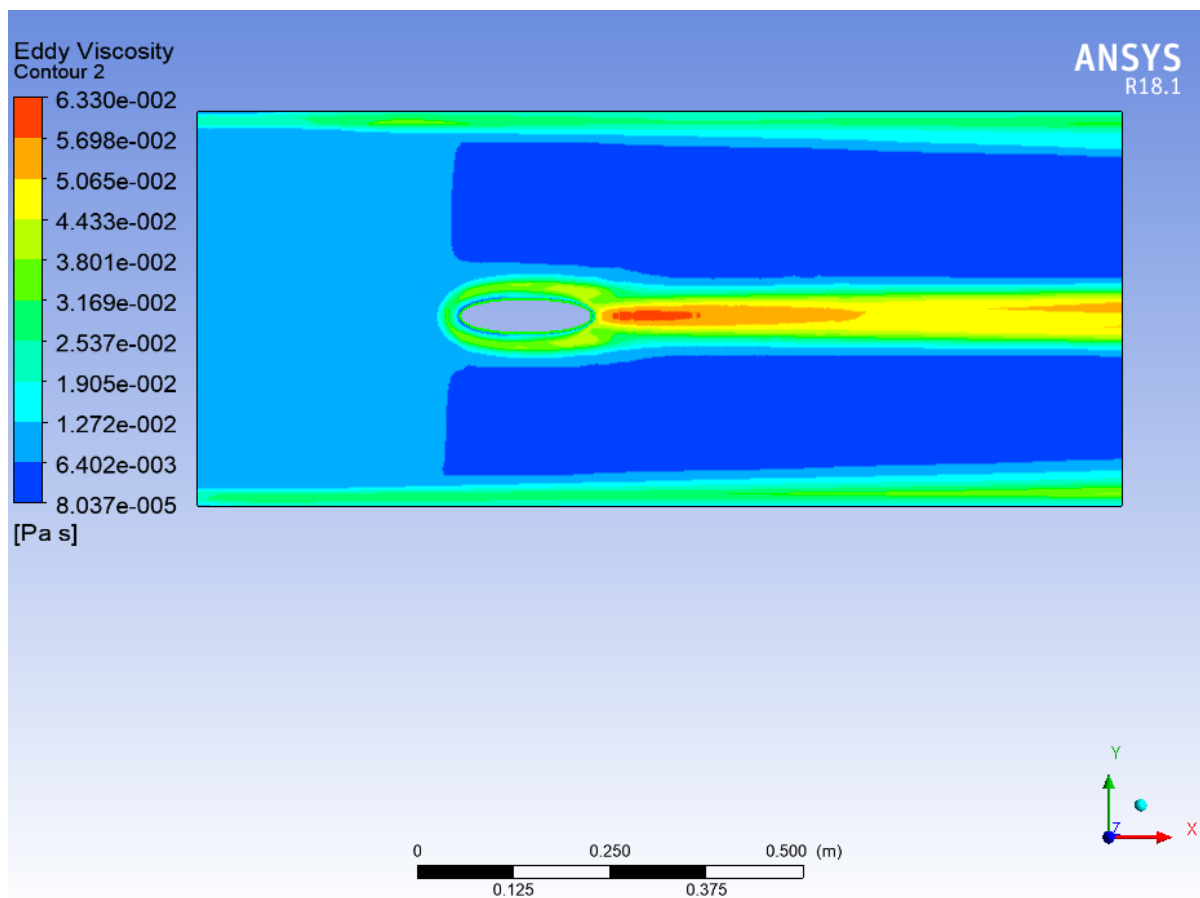

Figure A-5 Eddy Viscosity at X= 150mm (Mid-Wing)

Figure A 6 shows YX Plane Eddy Viscosity for standard K-Ɛ model for the velocity of 0.26 m/s at AOA = 2.
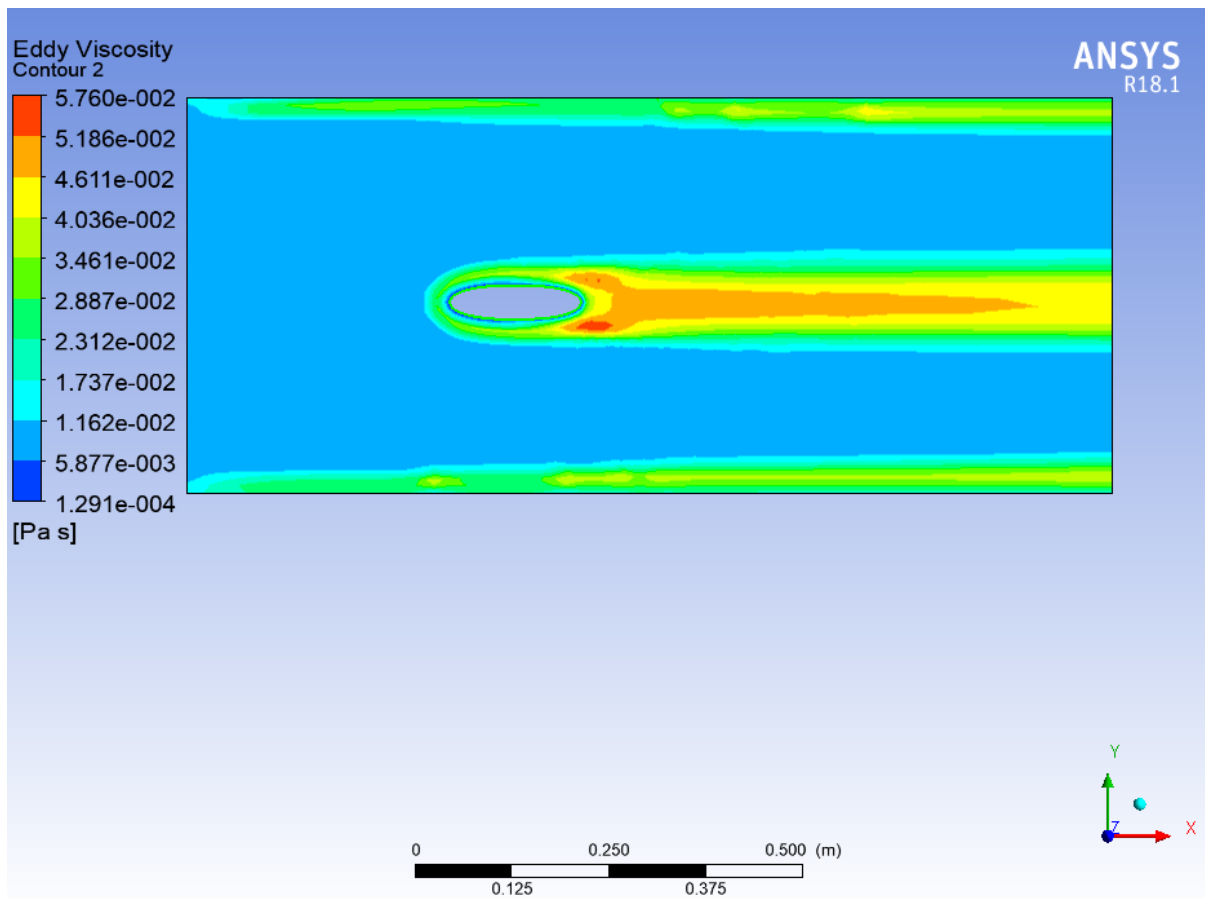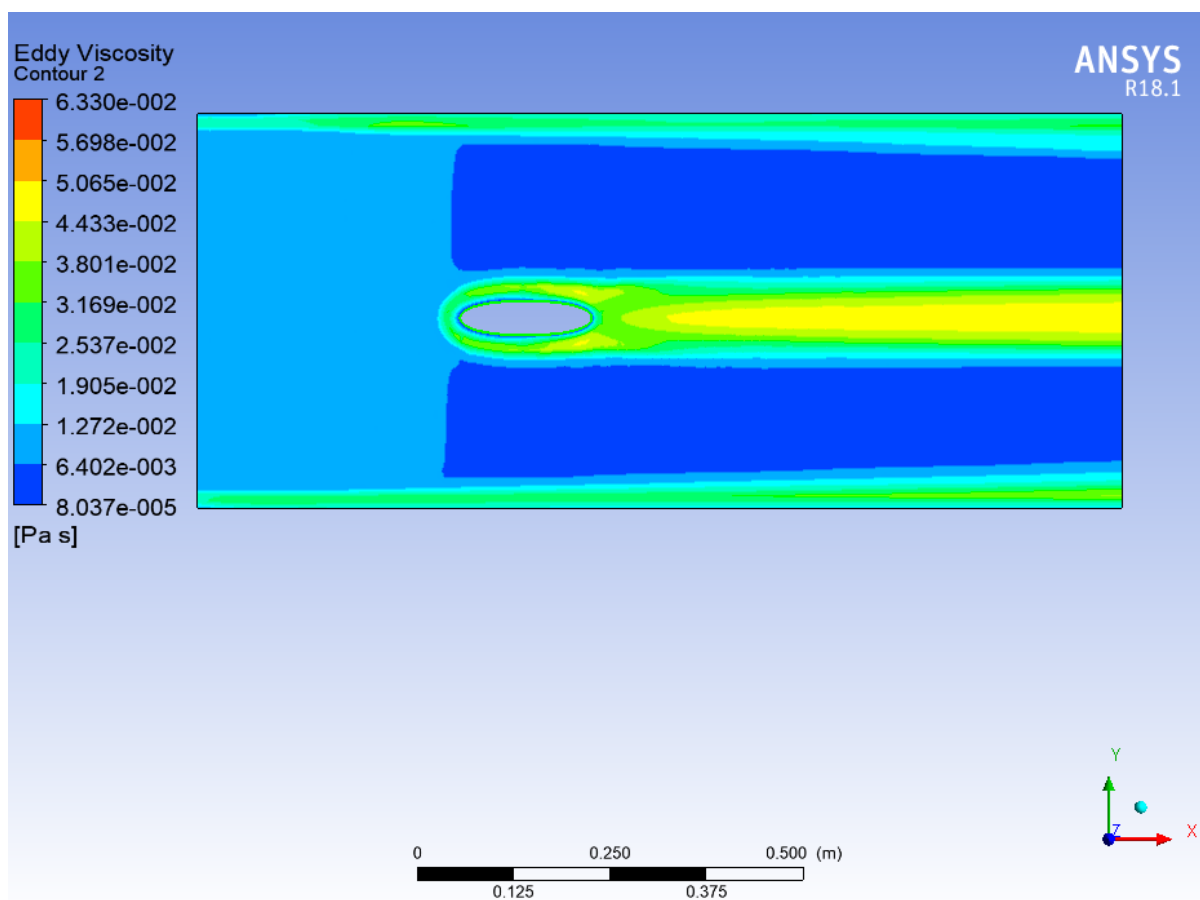

Figure A-6 Eddy Viscosity at X= 300mm (Tip-Wing)

APPENDIX B
STANDARD K-Ɛ(RNG) TURBULENT PARAMETERS RESULTS

TURBULENT KINETIC ENERGY RESULTS

Figure B1 shows YX Plane Turbulent Kinetic Energy for K-Ɛ -RNG model for the velocity of 0.26 m/s at AOA = 2.
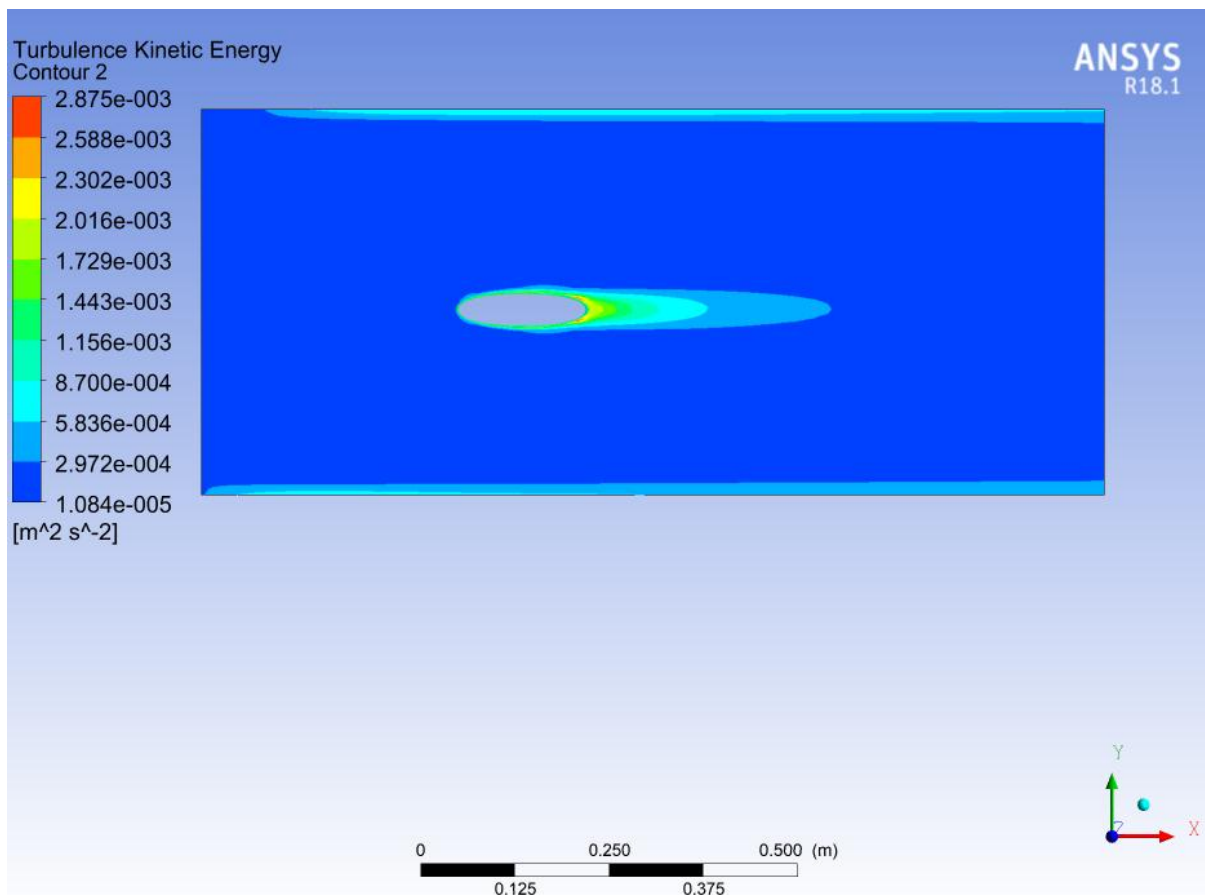

Figure B-1 Turbulent Kinetic Energy at X= 1mm (Close to the fuselage)

Figure B2 shows YX Plane Turbulent Kinetic Energy for K-Ɛ -RNG model for the velocity of 0.26 m/s at AOA = 2.

Figure B-2 Turbulent Kinetic Energy at X= 150mm (Mid-Wing)

Figure B3 shows YX Plane Turbulent Kinetic Energy for K-Ɛ-RNG model for the velocity of 0.26 m/s at AOA = 2.

Figure B-3 Turbulent Kinetic Energy at X= 300mm (Tip-Wing)

EDDY VISCOSITY RESULTS - K-Ɛ (RNG)

Figure B4 shows YX Plane Eddy Viscosity for K-Ɛ-RNG model for the velocity of 0.26 m/s at AOA = 2.

Figure B-4 Eddy Viscosity at X= 1mm (Close to the fuselage)

Figure B5 shows YX Plane Eddy Viscosity for K-Ɛ-RNG model for the velocity of 0.26 m/s at AOA = 2.

Figure B-5 Eddy Viscosity at X= 150mm (Mid-Wing)

Figure B6 shows YX Plane Eddy Viscosity for K-Ɛ-RNG model for the velocity of 0.26 m/s at AOA = 2.

Figure B-6 Eddy Viscosity at X= 300mm (Tip-Wing)

APPENDIX C
STANDARD K-Ɛ(REALIZABLE) TURBULENT PARAMETERS RESULTS

TURBULENT KINETIC ENERGY– K-Ɛ (Realizable) RESULTS

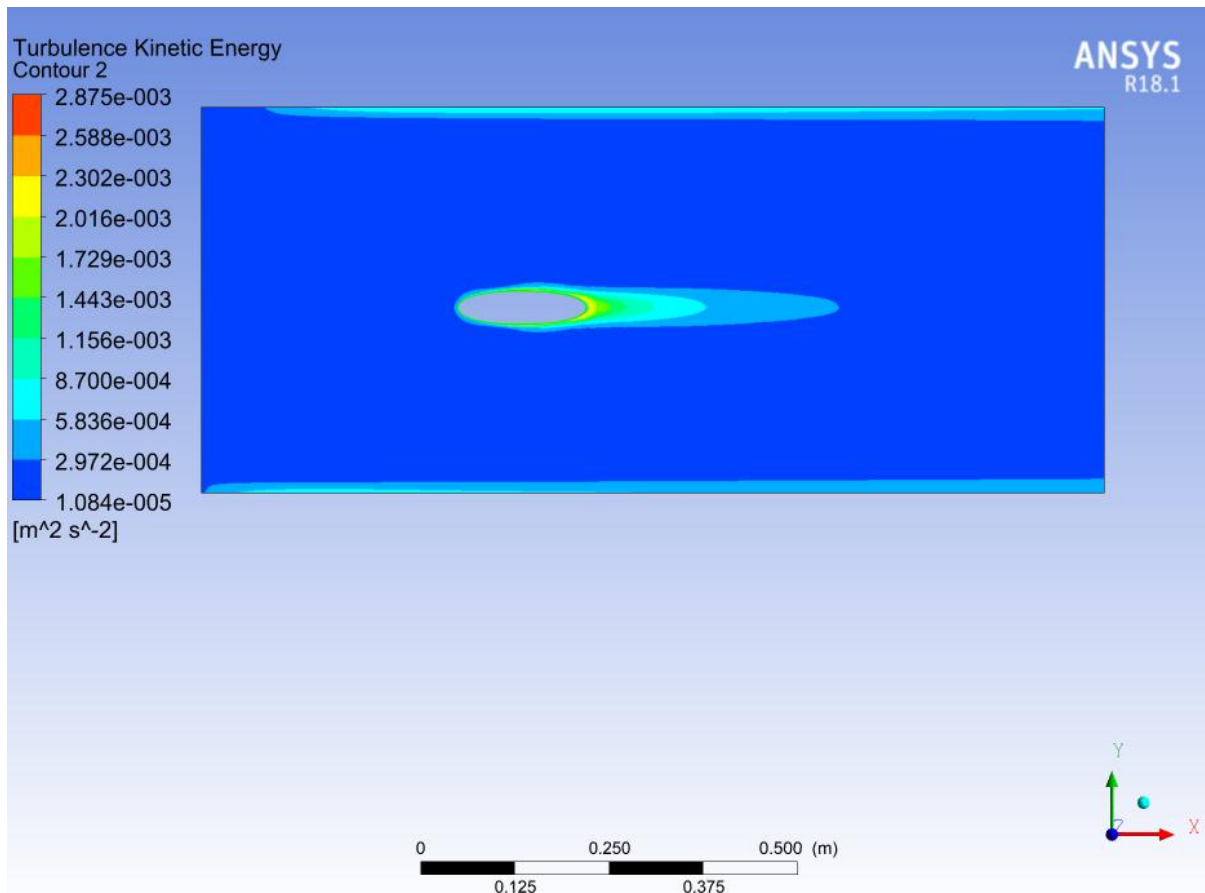Figure C1 shows YX Plane Turbulent Kinetic Energy for K-Ɛ -Realizable model for the velocity of 0.26 m/s at AOA = 2.

Figure C-1 Turbulent Kinetic Energy at X=1mm (Close to the fuselage)

Figure C2 shows YX Plane Turbulent Kinetic Energy for K-Ɛ -Realizable model for the velocity of 0.26 m/s at AOA = 2.

Figure C-2 Turbulent Kinetic Energy at X=150 mm (Mid-Wing)

Figure C3 shows YX Plane Turbulent Kinetic Energy for K-Ɛ -Realizable model for the velocity of 0.26 m/s at AOA = 2.
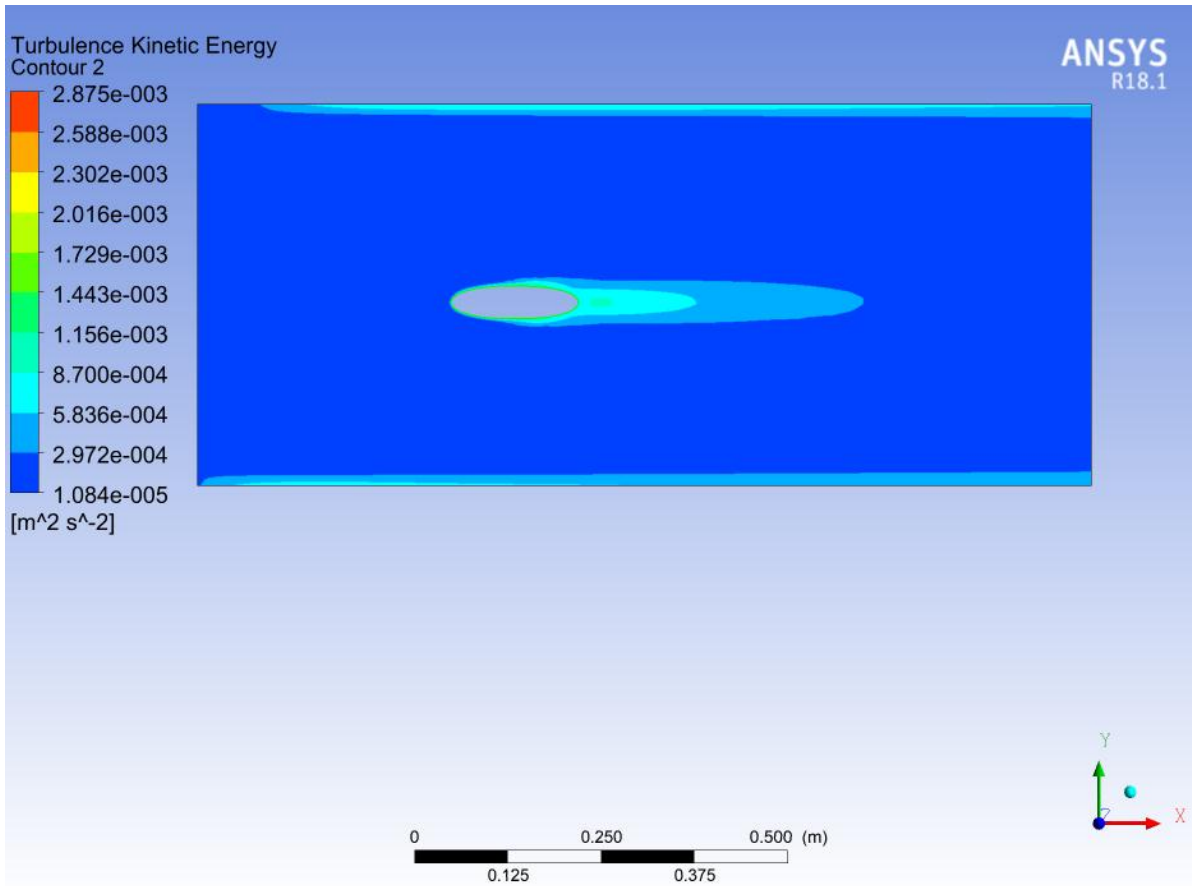

Figure C-3 Turbulent Kinetic Energy at X=300 mm (Tip-Wing)

EDDY VISCOSITY RESULTS - K-Ɛ (Realizable)

Figure C4 shows YX Plane Eddy Viscosity for K-Ɛ -Realizable model for the velocity of 0.26 m/s at AOA = 2.
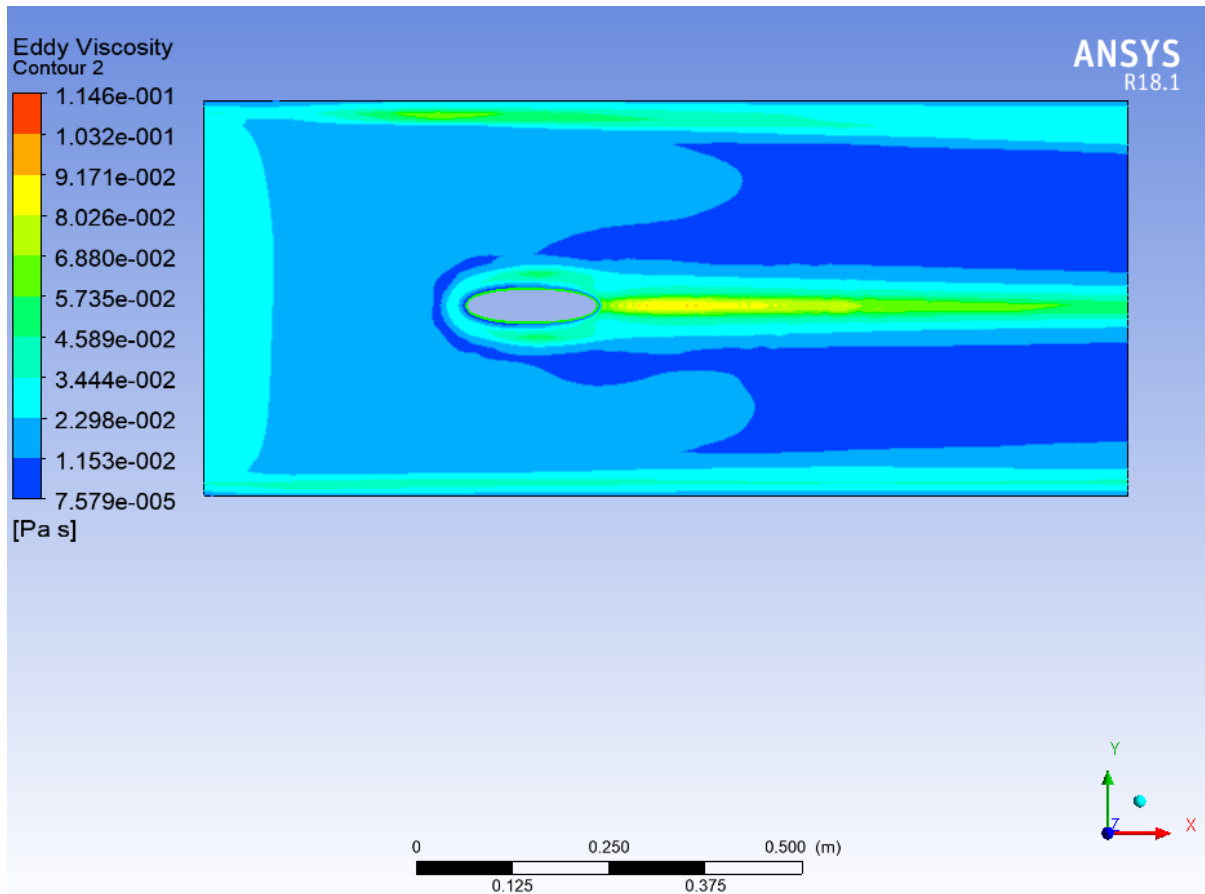

Figure C-4 Eddy Viscosity at X=1 mm (Close to the fuselage)

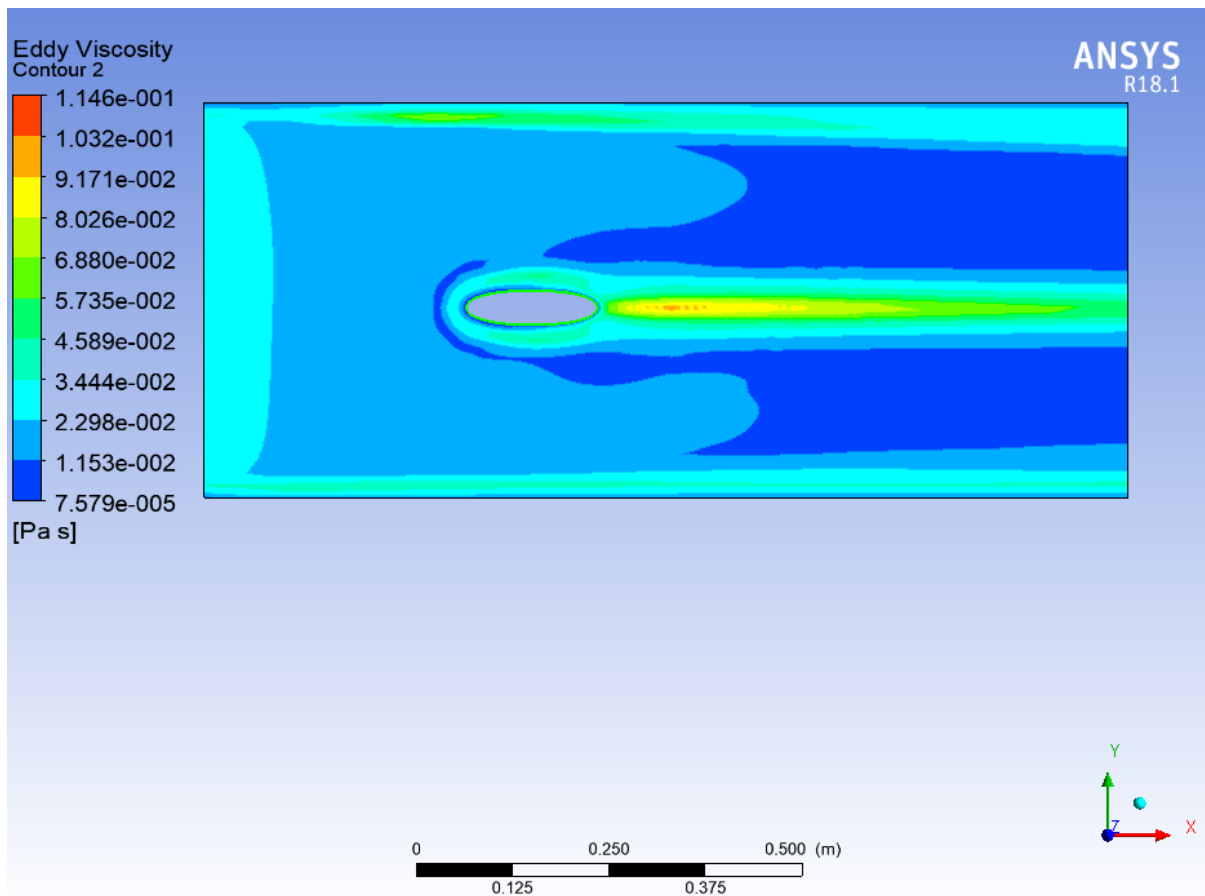Figure C5 shows YX Plane Eddy Viscosity for K-Ɛ -Realizable model for the velocity of 0.26 m/s at AOA = 2.

Figure C-5 Eddy Viscosity at X=150 mm (Mid-Wing)

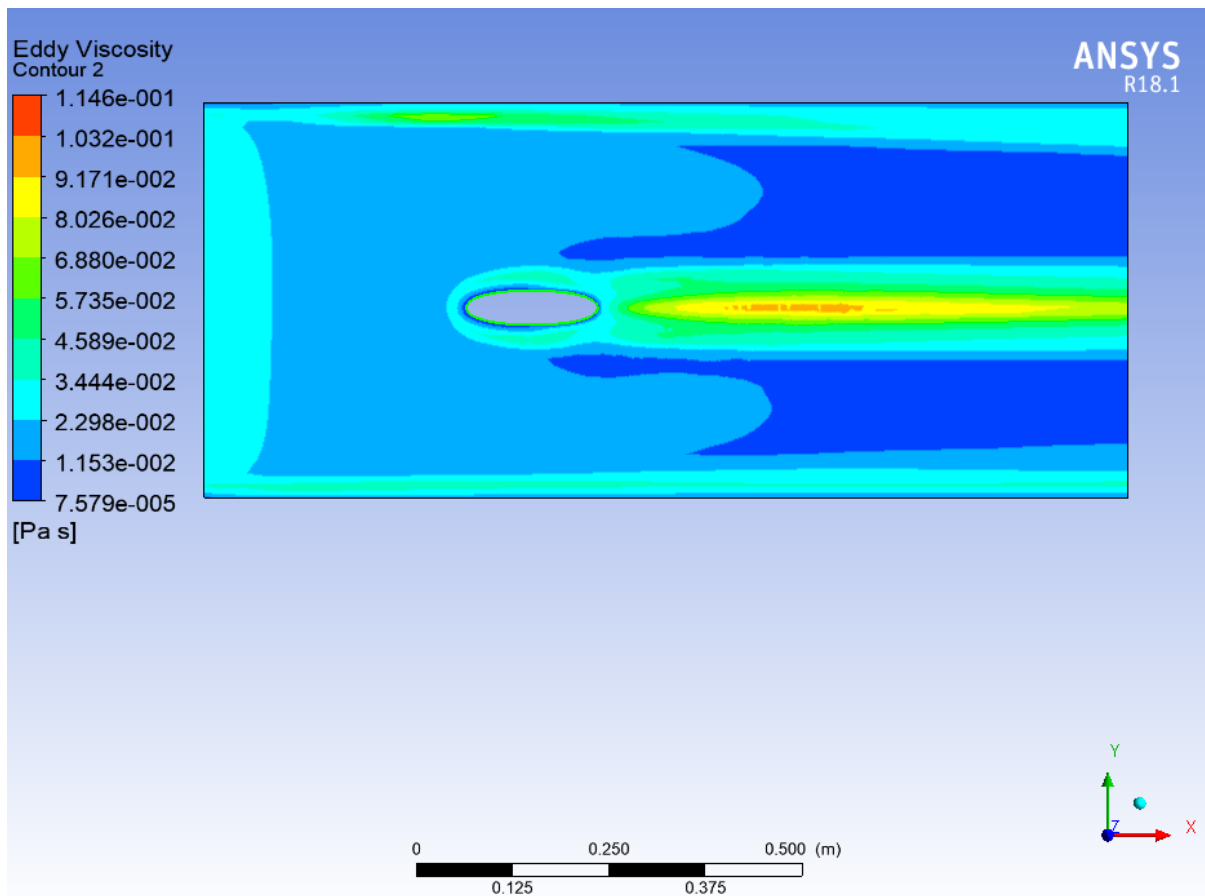Figure C6 shows YX Plane Eddy Viscosity for K-Ɛ -Realizable model for the velocity of 0.26 m/s at AOA = 2.

Figure C-6 Eddy Viscosity at X=300 mm (Tip-Wing)